

July 5, 2017

MASTER THESIS

Photoacoustic Tomography for Finger Joint Imaging: Tackling Artefacts

Daan de Muinck Keizer, BSc

**Faculty of Science and Technology
Biomedical Photonic Imaging Group**

Exam committee:

Supervisor

Prof.dr. Srirang Manohar

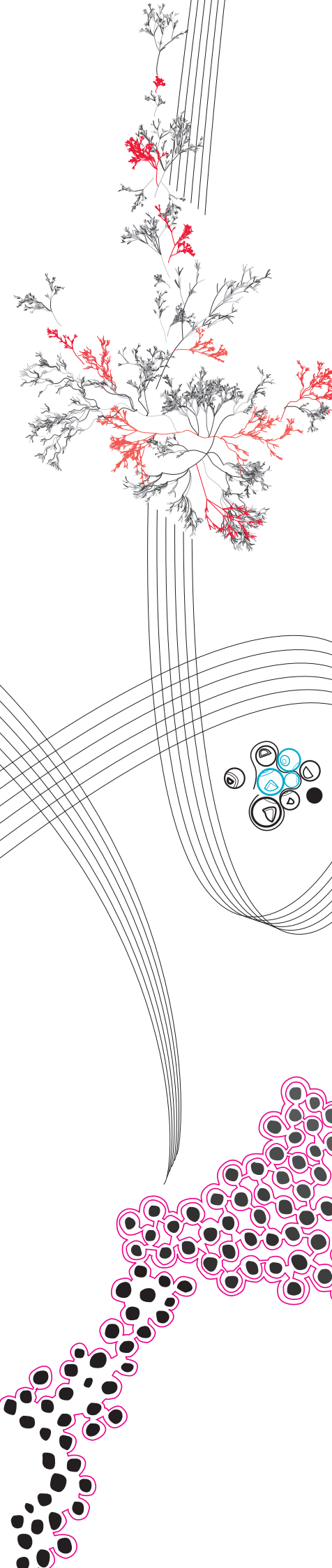
External committee member

Dr. Christoph Brune

Chairman

Prof.dr.ir. Wiendelt Steenbergen

UNIVERSITY OF TWENTE.



Abstract

Reumatoid Arthritis (RA) is an auto-immune disease which expresses itself as a chronic joint inflammation. The disease occurs most often in the small joints of hands and feet and causes inflammation in the synovium (joint lining) and can destroy articular tissues, causing pain and discomfort for the patient. It is currently not possible to prevent or cure RA, but most damage to the joints can be prevented or postponed if RA is diagnosed and treated in an early stage. The diagnosis of RA is normally performed with the help of radiography and the use of ultrasound (US). However, the drawbacks of those techniques is that they can only be used to visualize joint damage and are unable to detect RA in an early stage. It was found that there is a significant increase in the growth of blood vessels in an inflamed joint, affected by RA. Photoacoustic tomography is a promising and non-invasive imaging modality which is able to image small blood vessels in the finger with a high signal to noise ratio and can potentially be used to diagnose RA in an early stage.

Unfortunately, drawing conclusions from the photoacoustic images has proven to be challenging. Many artefacts are present on the images from which the origin and behavior are unknown. The presented work in this thesis shines new light on the artefacts observed in the images. The artefacts are investigated by theoretical explanation and simulating scenarios in which the artefacts occur. It was found that the major artefacts in the photoacoustic images arise due to acoustic pressures waves from blood vessels scattering and reflecting on the bone surface. It was also found that when the location of the blood vessels and the shape and size of the bone is known, the artefacts in the photoacoustic image can be predicted and replicated in simulations.

Additionally, a 3D visualization tool is presented which is able to visualize the blood vessels of an imaged patient finger. From the results of this tool it is possible to observe differences between the vascularity and density of the blood vessels in a healthy and an inflamed finger, which is in line with presented literature that states that the growth of blood vessels around inflamed joints increases. In future work, the visualization tool could be used in patient follow up to monitor the progression and growth of the blood vessels in an inflamed finger over time.

Preface

After returning from my internship in Australia, I've spend a full week researching possible graduation projections and found this assignment with BMPI. I was instantly hooked as it was an unprecedented opportunity for me to further develop the potential of the finger imager and gain more experience on developing imaging algorithms. I've found that developing algorithms with applications in medical imaging pleases me and I gain great satisfaction from the idea that my work contributes to innovations in the health care.

Although the initial idea of the assignment was to also conduct experiments with the finger imager, I underwent surgery which more or less impeded my experimental plans. Luckily, this posed no problem and I would like to sincerely thank my daily supervisor prof. dr. Srirang Manohar for his helpful insights, constructive criticism and providing me the freedom and trust to develop my own path to conduct research and develop solutions used for this assignment.

A thank you goes out to dr. Christoph Brune for being part of my examination committee and his interest in my work. Another thank you goes out to prof. dr. Wiendelt Steenbergen for allowing me to conduct research within BMPI, being the chairman of my examination committee and the constructive feedback during the work meetings. I thoroughly enjoyed working in BMPI and with its dynamic group of members.

Last, but not least, I would like to thank my friends and family. Mom and dad, for keeping faith in me and my dreams, even during the difficult times of my study. Gentlemen Ronald and Marten for providing the necessary laughs and distraction from daily life for more than a decade. My loving fiancee Corine for providing the never relentless support and motivation. I'm sincerely grateful and wouldn't be able to do it without you all.

Enschede, 12th June 2017

Daan de Muinck Keizer

Contents

1	Introduction	1
1.1	Rheumatoid Arthritis	1
1.2	Principle of Photoacoustics	3
1.3	State of the Art	8
1.4	Horizontal Tomography Finger Imager	9
1.5	Problem Statement	10
1.6	Thesis Layout	11
2	Potential Artefacts in PA Images	12
2.1	Biological Aspects	12
2.2	Hardware Aspects	20
2.3	Algorithm Aspects	21
2.4	Conclusion	24
3	Investigation of Clutter	25
3.1	Introduction to Monte Carlo simulations	25
3.2	3D Modelling	28
3.3	Implementation in k-Wave	35
3.4	Simulation of Monte Carlo Out of Plane data	38
3.5	Simulation of single projection	41
3.6	Discussion	43
3.7	Conclusion	44
4	Investigation of Acoustic Reflection	45
4.1	Simulation of numerical phantoms	45
4.2	Simulation of patient data	47
4.3	Discussion	53
4.4	Conclusion	54
5	3D Visualizations	55
5.1	Introduction	55
5.2	Algorithm Layout	55
5.3	Results	61
5.4	Discussion	64
5.5	Conclusion	65
5.6	Outlook	65
	References	66
	Appendix	69
A	Monte Carlo number of photons investigation	70
B	Effect of k-Wave filtering	73

Chapter 1

Introduction

In this introduction, information is provided about the disease Rheumatoid Arthritis, the principles of photoacoustics and the current state of the art of photoacoustic imaging. An overview of the finger joint photoacoustic tomography imager used in this research is also given.

1.1 Rheumatoid Arthritis

Rheumatoid Arthritis (RA) is an auto-immune disease which expresses itself as a chronic joint inflammation. RA is derived from the greek words *reuma* and *arthron*, where *reuma* has the meaning of flow or ill-making fluid and *arthron* is translated as joint [1]. The disease occurs most often in the small joints of hands and feet and causes inflammation in the synovium (joint lining) and can destroy articular tissues [2]. RA was determined to be the main cause of death of 175 persons in the Netherlands in 2015 [3]. A schematic overview of the effect of RA on a finger joint is given in figure 1.

In 2015 an estimated number of 234.400 persons in the Netherlands had the diagnosis RA. Of this group 86.200 (36.8%) were male and 148.200 (63.2%) female [4]. This means that 10 in 1000 men and 17 in 1000 women have RA. The costs of RA in the Netherlands in 2011 were 568 million euro in total [5].

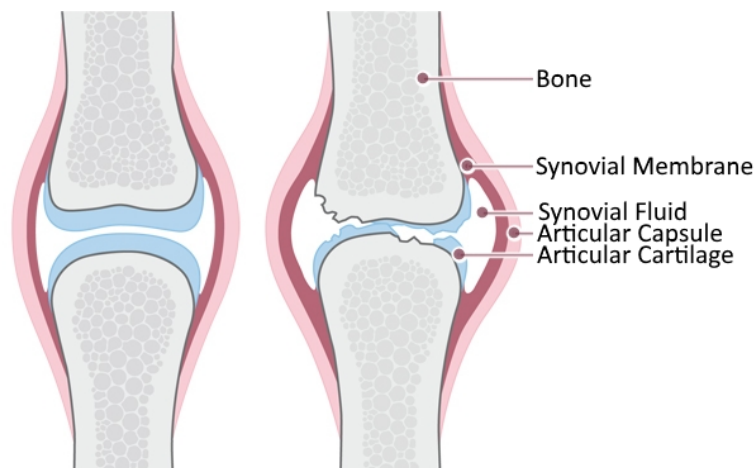


Figure 1: A schematic overview of the difference between a healthy joint and a joint affected by RA. The joint on the left hand side in the image resembles a healthy joint. The joint on the right hand side in the image shows an affected joint by RA where the synovial membrane is thickened and inflamed. The cartilage and the bone in the joint are eroded and have gained a rough and irregular shape [6].

Although not many risk factors for RA are known, it is suggested that genetic predisposition can play an important role in the expression of RA. The risk of developing RA is also elevated by smoking [7]. The fact that RA is more often found in women than in men could suggest that hormonal factors can play a role in developing RA. It is found that the risk of developing RA in women is reduced by breastfeeding for more than a year [8, 9].

It is currently not possible to prevent or cure RA. This is due to the fact that the cause of RA is unknown. There is no screening test available to test for RA with full certainty. It is important to note that most damage to the joints can be prevented or postponed if RA is diagnosed and treated in an early stage [1].

RA is diagnosed with the help of blood tests, a physical exam according to the 2010 ACR-EULAR-criteria (American College of Rheumatology and European League against Rheumatism) and with the help of imaging [10]. The blood tests are examined for inflammation levels and presence of antibodies which can be linked to RA. The physical exam can diagnose RA if there is atleast one inflammation in a joint and if there are no other diagnoses which can explain the inflammation in the joint.

Imaging in diagnosis of RA is normally performed with the help of radiography and the use of ultrasound (US). Radiography is used to determine the degree of joint destruction and to determine the joint space width, where US is used to visualize thickening of the synovium and fluid build-up in progressed RA [11, 12]. US Doppler has the ability to visualize flow in soft tissues and can be used to image the local inflammation in the joint. The drawbacks of those imaging techniques is that they are unable to detect RA in an early stage.

1.1.1 Angiogenesis and RA

There is a significant increase of vascular density in the synovium of joints affected by RA [13]. The growth of new blood vessels in affected joints is caused by multiple factors. One of the main factors is that the inflamed joint has an increased metabolic rate, which in turn, causes local oxygen shortage (or hypoxia). These two factors combined induce angiogenesis, the creation of new blood vessels. These blood vessels transport new pro-inflammatory cells to the joint, which in turn, increase the inflammation [14, 15].

The imaging and visualization of the blood vessels in the finger can play an important role in the early diagnosis of RA and the determination of the progression and state of the disease. Photoacoustic tomography is a promising non-invasive imaging modality which is able to image the microvasculature in the finger with a high signal to noise ratio which makes that this research focuses on imaging fingers with the help of photoacoustics.

1.2 Principle of Photoacoustics

Photoacoustic imaging is based on the photoacoustic effect: the generation of acoustic pressure waves from the absorption of time-variant electromagnetic energy. Or in a more simplistic way, the generation of sound by absorbing light in tissue [16].

Figure 2 gives an overview of the process of the photoacoustic effect. This process starts with irradiating tissue with a pulsed laser. Light is absorbed by the tissue, which causes a local temperature rise. The temperature rise leads to thermoelastic expansion and a build up of pressure. This is the initial pressure, or p_0 . The built-up pressure in the tissue will then propagate as a pressure wave; this propagating wave can then be detected with the help of an ultrasound detector. The photoacoustic effect is also schematically shown in Figure 3.

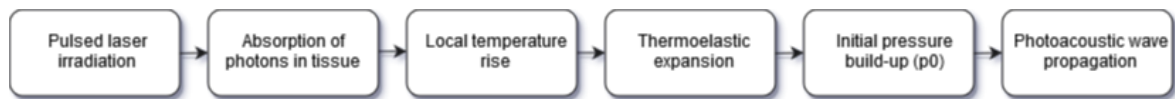


Figure 2: Schematic overview of the photoacoustic process.

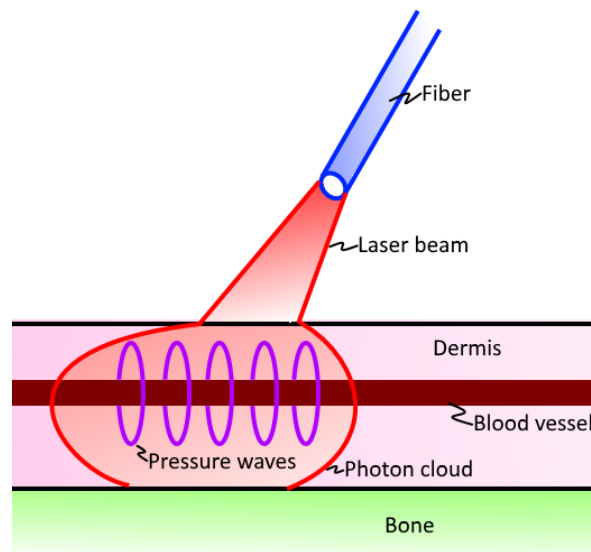


Figure 3: Schematic example of the photoacoustic effect with a laser beam emitting from a fiber and irradiating on tissue. This tissue consists of the dermis, a blood vessel and bone. In this example, the photons from the laser beam are absorbed by the blood vessel. The absorbed energy in the blood vessel increases the local temperature, which then gives rise to a thermal elastic expansion. And as a result, pressure waves are emitted from the blood vessel.

The generation of the photoacoustic effect depends on two important conditions: the thermal and stress confinements. The thermal confinement (τ_{th}) states that the laser pulse duration should be shorter than the heat diffusion of the tissue voxel. This relation is given in equation 1.

$$\tau_{th} < \frac{L_p^2}{4D_T} \quad (1)$$

With L_p in $[m]$ as the size of the tissue voxel being heated and D_T in $[m^2/s]$ as the thermal diffusivity of the particular tissue. The stress confinement states that the laser pulse duration should be shorter than the time it takes for the built-up stress to leave the heated tissue voxel. This relation is given in equation 2.

$$\tau_s < \frac{L_p}{c} \quad (2)$$

With c in $[m/s]$ as the speed of sound in tissue. Combining both confinements leads to the laser pulse duration that results in the most optimal photoacoustic effect. This relation is given in equation 3.

$$\tau_p < \frac{L_p}{c} < \frac{L_p^2}{4D_T} \quad (3)$$

Now that both confinements are set, the initial pressure which arises from the absorbed energy in the tissue can be calculated. This relation is given in equation 4.

$$p_0 = \Gamma Ea = \left(\frac{\beta c_s^2}{c_p}\right) (\phi \mu_a) \quad (4)$$

With p_0 as the initial pressure, Γ (*gamma*) as the dimensionless Grüneisen coefficient, Ea in $[J/m^3]$ as the absorbed energy in the tissue voxel, β in $[K^{-1}]$ as the thermal expansion coefficient, c_s as the speed of sound in the tissue, c_p in $[J/(Kkg)]$ as the thermal heat capacity of the tissue, ϕ in $[J/m^2]$ as the fluence, and μ_a in $[cm^{-1}]$ as the absorption coefficient of the tissue. This relation shows that the initial pressure can be described by a function of the absorbed energy Ea and the characteristic Grüneisen coefficient of the irradiated tissue [16].

1.2.1 Imaging Quality of Photoacoustics

Photoacoustic tomography (PAT) has some important advantages over magnetic resonance imaging (MRI) and US imaging. And, as previously stated in the introduction, of these three imaging modalities is PAT the only one able to image the microvasculature in the finger with a high signal to noise ratio [17].

An overview of the differences in resolution and depth of the different imaging modalities is given in Table 1.

Table 1: *Overview of the resolution and depth in different imaging modalities [17].*

Modality	Resolution (μm)	Depth (mm)
PAT	5-800	0.7-50
MRI	1000	100-200
US	500-1000	100-200

MRI with injected contrast agents can be used to image the blood vessels (*angiography*) in the hand of the patient. The downside to this technique is that it is relatively expensive, time consuming and requires the administering of contrast agent in the blood circulation of the patient [11].

The imaging depth of PA depends on the penetration depth of the photons in the tissue. The penetration depth is also depending on the used wavelength of the irradiating laser beam. Photons penetrating the tissue will be scattered and absorbed by light absorbing molecules, which are called *chromophores* [18].

The most optimal penetration is achieved at around 800 nm, as this is the isobestic point where the two extinction spectra of oxygenated and de-oxygenated blood intersect [16]. Figure 4 gives an overview of the extinction spectra of oxygenated (HbO_2) and de-oxygenated (Hb) blood.

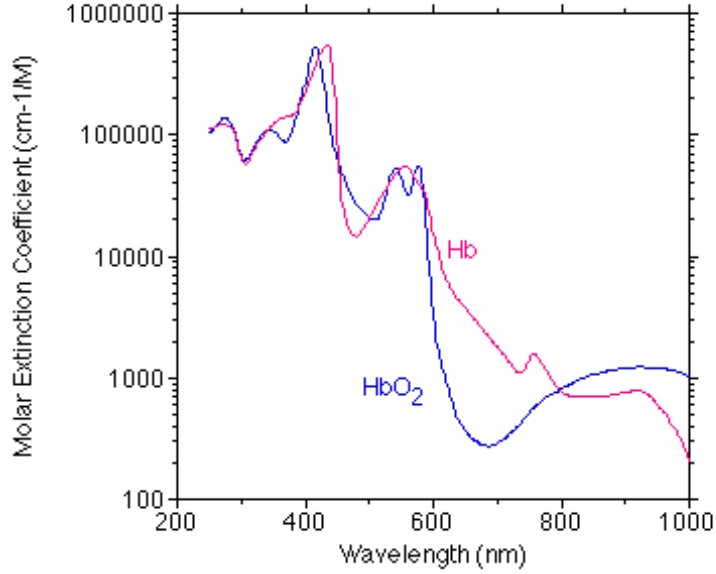


Figure 4: Extinction spectra of oxygenated (HbO_2) and de-oxygenated (Hb) blood. There is an intersection visible at the wavelength of 800 nm [19].

The penetration and thus the imaging depth is limited by the effective attenuation coefficient (μ_{eff}) of tissue. The coefficient μ_{eff} is defined by the absorption (μ_a) and reduced scattering coefficient (μ'_s) of the tissue [18]. The relation of μ_{eff} is given in equation 5. Both μ_a and μ'_s are given in [cm^{-1}]. The relation of μ'_s is given in equation 6.

$$\mu_{eff} = \sqrt{3\mu_a(\mu_a + \mu'_s)} \quad (5)$$

$$\mu'_s = \mu_s(1 - g) \quad (6)$$

With μ_s the scattering coefficient of the tissue in [cm^{-1}] and g the anisotropy factor. The anisotropy factor describes the scattering direction of a photon upon hitting a particle. The factor is described by a value between -1 and +1, which determines the general direction of scattering of the photon. A value of +1 represents straight forward scattering of photons, while -1 represents backward scattering.

1.2.2 Reconstruction algorithms

After the measurement has been performed, the photoacoustic image is reconstructed from the recorded acoustic signals. The reconstruction algorithm used has a strong influence on the resulting image quality of the photoacoustic image [20]. Examples of algorithms used for the reconstruction of two-dimensional PA images are the spatial Fourier-transform reconstruction algorithm [21], filtered back-projection [22] and time reversal [18]. Iterative based reconstructions are also being researched in an attempt to improve image quality [23].

The algorithms that will be discussed in this section are filtered back-projection (FBP) and time reversal (TR). The FBP algorithm is utilized to reconstruct the photoacoustic images of the finger imager used in this research. The TR algorithm is used to reconstruct the photoacoustic images in simulations performed for this research, as discussed in section 4.2 of this report.

The TR algorithm is based on the principle of back propagating time-reversed signals, which have been recorded by ultrasound detectors. These signals are reversed in time to reconstruct the initial pressure from which the photoacoustic image is formed. The algorithm fully functions within the domain of the wave equation [24]. TR is a versatile algorithm, as the speed of sound in the medium can be variable and thus reconstructing photoacoustic images of inhomogeneous media is possible [25].

The FBP algorithm, in contrast to TR, is a geometrical approach and not based on the wave equation. The principle of backprojection is given in Figure 5. The ultrasound array elements (labeled r) detects the pressure waves at a time t . The recorded signals of all detector elements are then backprojected with a speed of sound c along the curve with distance ct to reconstruct the initial pressure [18].

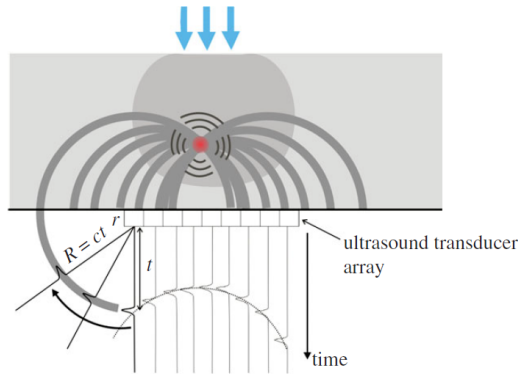


Figure 5: Principle of backprojection with a planar detector. The ultrasound array elements (labeled r) detects the pressure waves at a time t . The recorded signals of all detector elements are then backprojected with a speed of sound c along the curve with distance ct to reconstruct the initial pressure [18].

Contrast differences seen between FBP and TR are negligible. Both algorithms have the same imaging resolution, as proven by Zhang et al. [25] Because there is no significant difference in the resulting images from both algorithms, the images resulting from the simulation in section 4.2 of this report may be compared with the original photoacoustic images of the patient measurements by Zwiers [26] and Vlieg [27].

1.3 State of the Art

Previous work used in this research is performed by Van Es [12, 28, 29], who developed a vertical finger imager. A problem with this imager was that the machine suffered from movement artefacts and unstable data processing hardware [27]. A new finger imager was built in an attempt to solve these problems. This new imager is the horizontal tomography finger imager (HTFI) (described in section 1.4). Technical and structural improvements on the HTFI were performed by Vlieg [27]. Studies with finger phantoms and the influence of tilt on blood vessels and artefacts seen on reconstructed photoacoustic images were conducted by Zwiers [26].

Photoacoustic imaging is applied in many different research areas. Photoacoustic tomography for example is used in small animal imagers [30] and breast imaging [31]. Other research groups, such as the group of Wang [32], are also working on imaging fingers with the help of photoacoustics.

Both the HTFI and the finger imaging system of the group of Wang [32] use an Nd:YAG pulsed laser system with a repetition rate of 10 Hz and a pulse width of 5 ns. However the HTFI uses a wavelength of 800 nm, while Wang et al. use a wavelength of 580 nm [33]. The main difference between both systems is that HTFI works with a curved 64 element ultrasound array covering 172 degrees at a center frequency of 7.5 MHz, while the system of Wang et al. use a linear array with 128 elements and a center frequency of 11.25 MHz. The HTFI is able to image arteries and veins from $100\mu\text{m}$ up to sizes of 1.5 mm. Details of the skin, such as the epidermis and the subpapillary plexus are also visible [29]. Wang et al have no recently reported numbers of achievable resolution, but reported that their system performance is comparable with the performance of a clinically available Doppler US system when identifying inflammation in finger joints [34].

Current research in the field is focused on further improving the sensitivity and specificity of photoacoustic imaging of finger joints. Research is also being conducted on multi-spectral photoacoustic imaging, which makes use of multiple optical wavelengths for an improved differentiation between bone, blood vessels and joint tissues [33].

1.4 Horizontal Tomography Finger Imager

The HTFI is capable of US imaging and photoacoustic imaging. The US detector element consists of two arrays with a center frequency of 1.5 MHz and 7.5 MHz, mounted next to each other. Both arrays have 64 detection elements and cover 172° of a circle. Both arrays are capable of US imaging, as the 7.5 MHz array has 12 ultrasound pulsers and the 1.5 MHz has 8 ultrasound pulsers, all placed between the detector elements. A single detector element of the 7.5MHz has a size of 9.5 mm in length and a width of 0.5 mm. The spacing between elements is 1.2 mm.

An overview of the system is given in Figure 6. This figure shows two photographs of the system with a side and frontal view. The important features of the system such as the finger support, fibers and US array are highlighted.

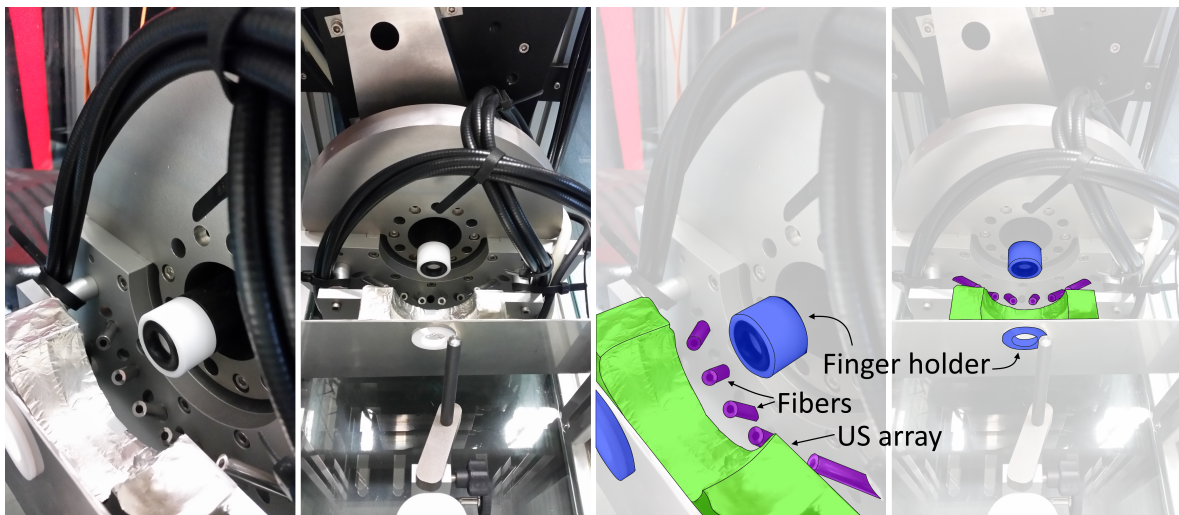


Figure 6: Photographs of the HTFI system. The white Teflon ring in the middle of both photographs provides support for the subjects fingertip. Directly beneath the Teflon ring are the fibers and the ultrasound array, covered with a sheet of aluminium foil. Photographs used with permission of Zwiers [26].

Figure 7 shows the setup of the illumination fibers and the coverage of the ultrasound array from both the frontal view as the side view. The fibers are arranged in such a way that they can illuminate 180° of the finger and the ultrasound array is able to image 172° of the finger. The ultrasound detector elements of the ultrasound array are shown as the black squares.

The imaging system is built in an aquarium, which is filled with water prior to measurements. The water is used as a coupling layer between the skin and the ultrasound detectors. The system also features an adjustable arm rest, which allows for comfortable positioning of a subject's arm during measurements.

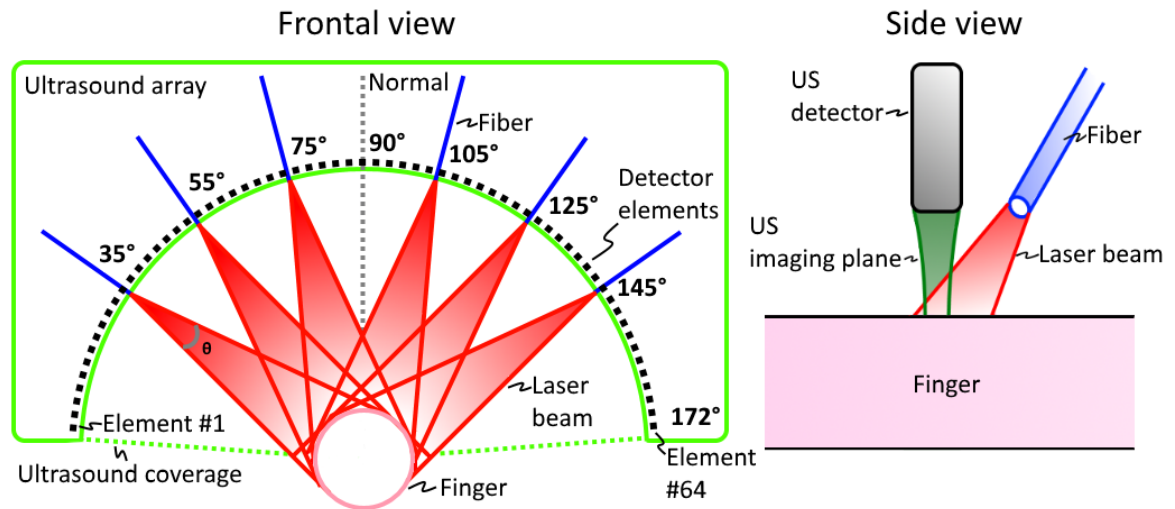


Figure 7: The setup of the illumination fibers and the ultrasound array. The image on the left hand side provides a frontal view. The fibers are shown as the blue lines. The detector elements inside the ultrasound array are shown as the black squares. The image on the right hand side shows the side view of the setup.

1.5 Problem Statement

The main goal of this thesis is to understand and reduce artefacts in 2D photoacoustic imaging of finger joints. Images obtained with the horizontal finger imager can carry so-called streak artefacts of which the cause and behavior is unknown. An example of a streak artefact is given in figure 8, where a cross-sectional photoacoustic image of a finger is shown, obtained with the HTFI [27].

Two small sections of the image are zoomed in and shown an example of the streak artefacts. A hypothesis is these image features are blood vessels meandering towards the bone in the center of the finger. A second hypothesis is that the artefact arises due to reflection of ultrasound pressure waves on the bone surface in the finger.

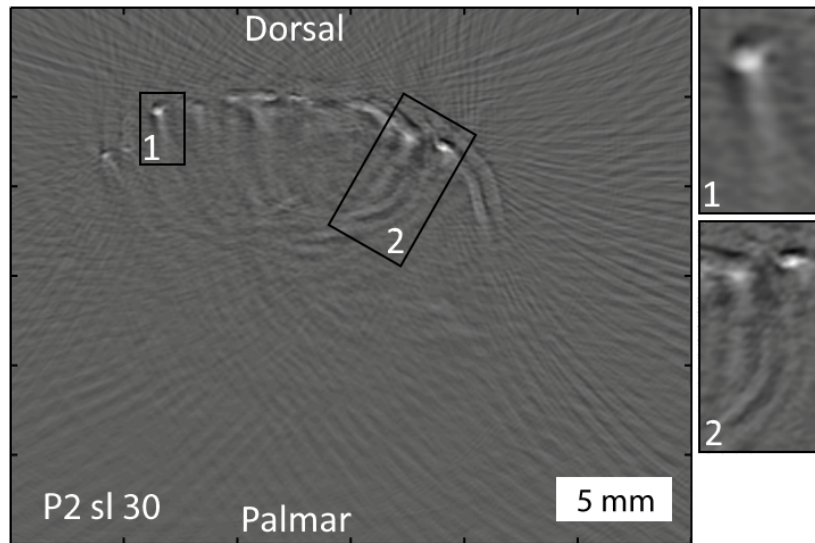


Figure 8: *An example of a cross-sectional photoacoustic image of a finger, obtained with the HTFI. The image shown is the result of the measurement of patient 2, slice 30, performed by Zwierny [26]. Two small sections of the image are enhanced and these are examples of so-called streak artefacts.*

1.6 Thesis Layout

This thesis describes the various steps and experiments performed to investigate the aforementioned problem:

- A theoretical description of the potential artefacts, considering imaging instrument characteristics and finger joint characteristics.
- Development of models and simulations to investigate the origin of the artefacts and reduce these. The simulations include investigation of absorption of light in tissue, out of plane clutter and acoustic reflection.
- Investigation and implementation of 3D visualization of the 2D slice data, to help discrimination between branching vascular networks and artefacts. A selection method in the 3D rendering method that discards the photoacoustic signal from the skin surface is also considered.

Chapter 2

Potential Artefacts in PA Images

The goal of this chapter is to provide insight into important artefacts which can occur in PA images of finger joints. Artefacts seen in the reconstructed PA images can have biological, hardware and/or algorithm origins.

2.1 Biological Aspects

Artefacts which have a biological origin can be hard to tackle, as their shape, size and intensity can differ for small changes in anatomy. The following paragraphs discuss clutter, acoustic reflection and tilt artefacts.

2.1.1 Clutter

Clutter arises from acoustic signals outside of the imaging plane and projects non-existent objects in the reconstructed image. Clutter can be divided into two main categories, namely *direct clutter* and *indirect clutter* (or *echo-clutter*).

The term *direct* clutter is used for acoustic signals that reach the detector without additional scattering or reflection. The term *indirect* clutter is used for acoustic signals that are reflected on acoustic scatterers or reflectors (such as bone) before the signals reach the detector [35].

Figure 9 provides a schematic overview of the origin of clutter. Two arrows are shown, labeled direct and indirect clutter. The effect of clutter in the setup of the HTFI is investigated and simulated in section 3.4.

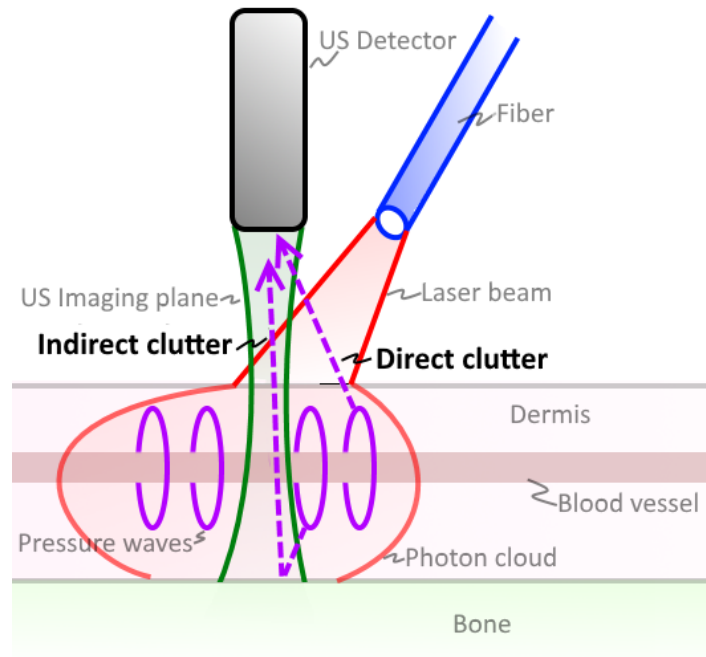


Figure 9: A schematic overview of the photoacoustic setup in the HTFI and the origin of clutter. Two arrows are shown, labeled direct and indirect clutter. The arrow labeled direct clutter shows an example of a detected signal that directly originates from a source outside the imaging plane. The arrow labeled indirect clutter shows an example of a signal from a source outside the imaging plane that is first reflected by bone and then detected.

2.1.2 Ultrasound Reflection Artefacts

Reflection of acoustic waves occurs due to the large difference in material properties between the soft tissue and bone. An example of acoustic reflection is given in Figure 10. This figure shows the reflection of an initial pressure wave on bone surface and the detection of both pressure waves by an ultrasound detector.

Figure 11 gives a schematic example of the detected pressure in the US detector displayed in Figure 10. The figure shows that the initial pressure wave from the blood vessel is detected first with and has the highest intensity. The reflected wave is detected later, and has a lower amplitude due to acoustic attenuation. The resulting reconstruction is shown in Figure 12. Two blood vessels are shown in the figure as effect from the acoustic reflection.

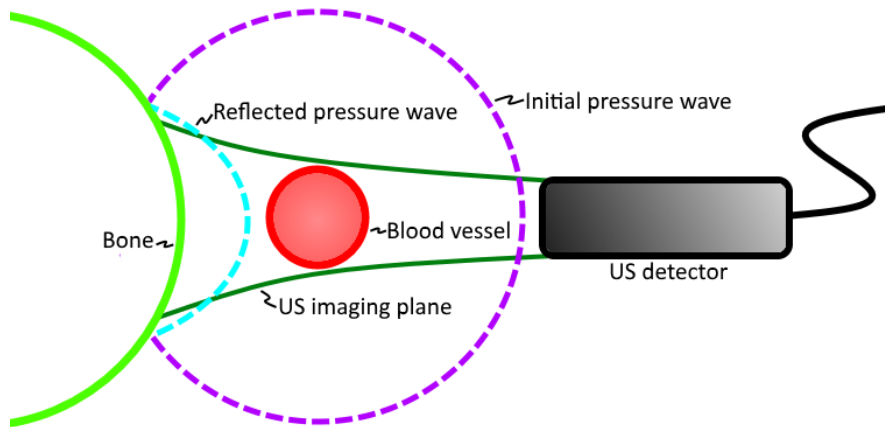


Figure 10: A schematic example of acoustic wave reflection. A pressure wave originating from the blood vessel is shown which is reflected by the bone surface. The US detector on the right hand side will detect the initial pressure wave from the blood vessel first, and then the reflected pressure wave.

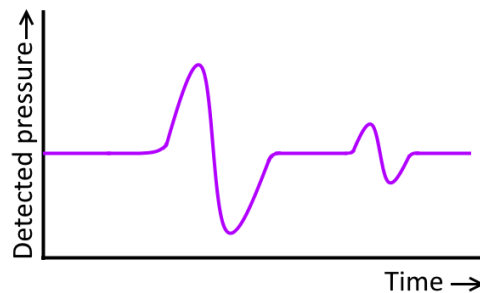


Figure 11: A schematic example of the detected pressure in the US detector given in Figure 10. The y axis resembles the pressure detected and the x axis the time. The initial pressure wave from the blood vessel is detected first, and has the highest energy. The reflected wave is detected later, and has a lower amplitude due to acoustic attenuation.

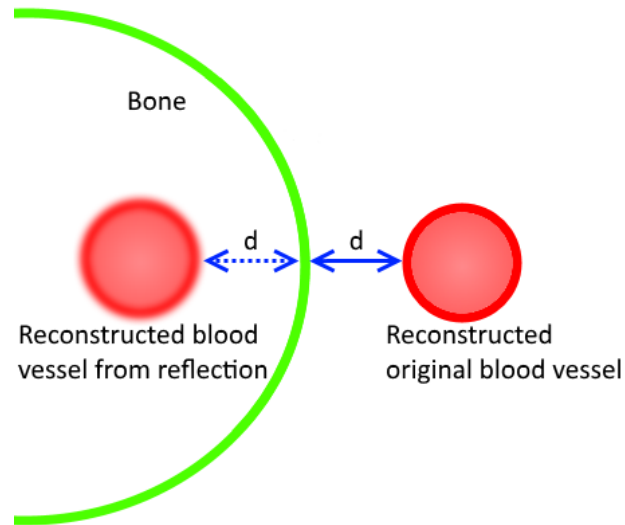


Figure 12: *An example of the reconstruction resulting from Figure 10. This figure shows the reconstructed original blood vessel on the right hand side and also shows a reconstructed, but non-existent, blood vessel inside the bone due to acoustic reflection.*

Another type of reflection artefacts is shown in Figure 13. This figure shows the pressure wave of a blood vessel from outside the imaging plane, reflected on bone before reaching the detector. The blood vessel is then falsely reconstructed (or projected) inside the bone. This artefact can also be classified as an indirect clutter artefact due to the fact that the signal originates from outside the imaging plane.

Figure 14 shows a schematic example of how a streak artefact is formed. A real blood vessel is shown in the figure, which emits an initial pressure wave that is scattered and reflected by the (rough) bone surface. The different ultrasound detectors resemble three detector elements of the detector array used in the HTFI and detect the scattered and reflected pressure waves. During reconstruction of the PA image, the recorded signal is projected along straight lines and the combined projections of the scattered and reflected signals form the streak artefact.

The effect of acoustic reflection artefacts and its behavior is investigated in section 3.

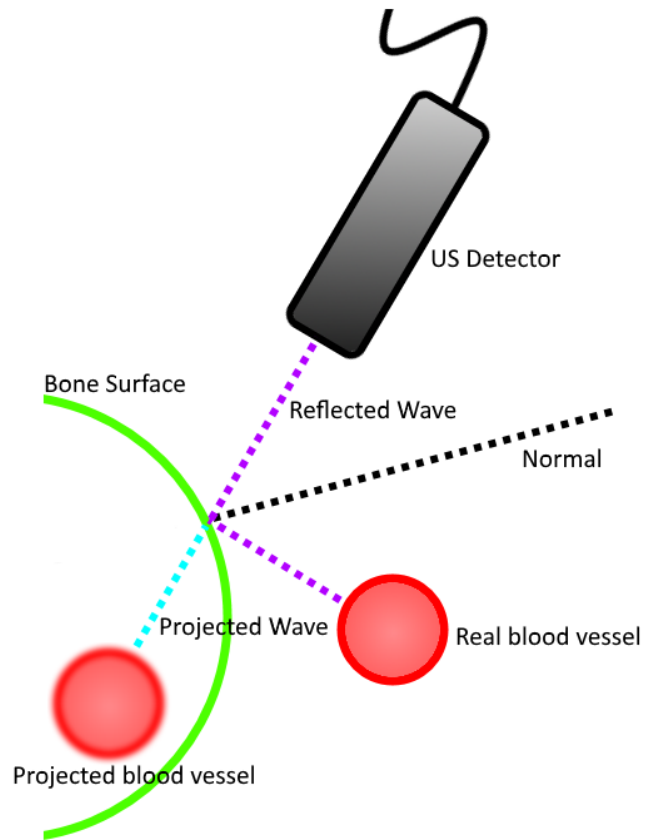


Figure 13: *The pressure wave of a blood vessel from outside the imaging plane is shown. The pressure wave of the blood vessel reflects on the bone surface and then reaches the detector. The blood vessel is then falsely reconstructed (or projected) inside the bone. The example shown can also be called indirect or out of plane clutter.*

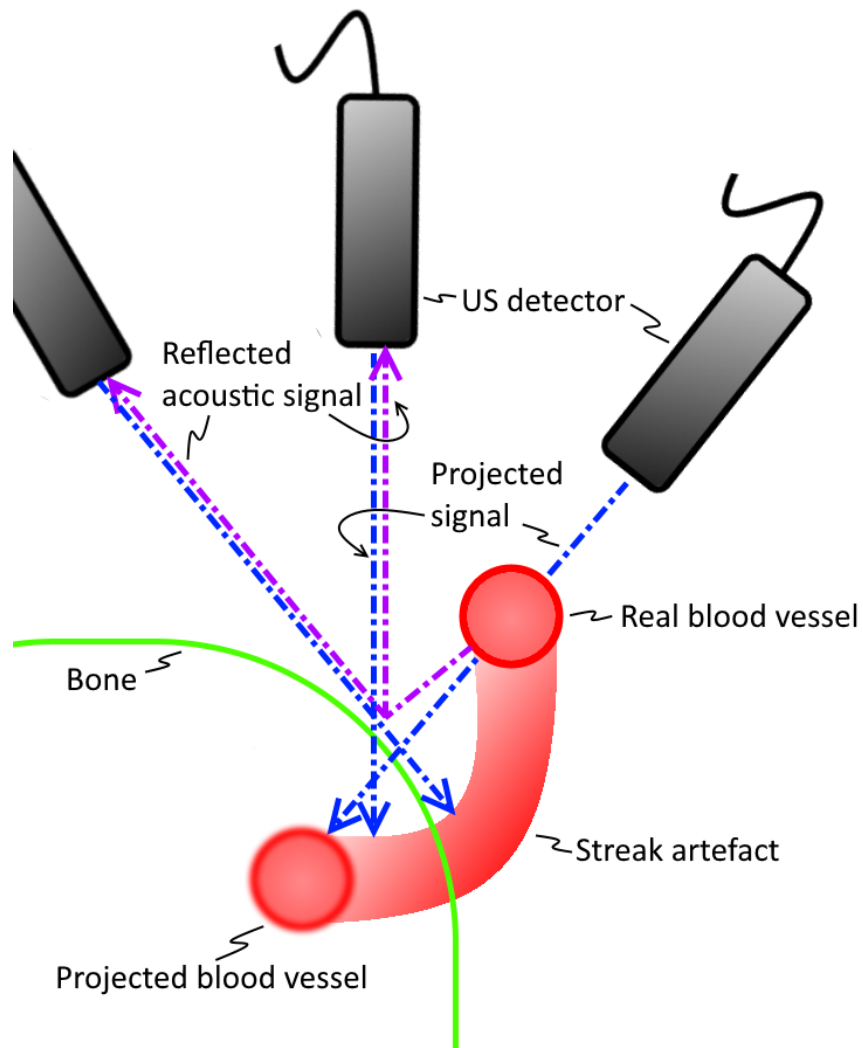


Figure 14: Principle of streak artefacts occurring due to acoustic reflection on bone. The figure shows a real blood vessel, which emits an initial pressure wave. This pressure wave is scattered and reflected by the (rough) bone surface. The scattered and reflected acoustic pressure waves are recorded by different US detectors which resemble detector elements of the US array in the HTFI. During reconstruction of the PA image, the recorded (scattered and reflected) signal is then projected along straight lines. The combined projections of the scattered and reflected signals form the streak artefact.

2.1.3 Tilt

The effect of blood vessels tilt in the horizontal plane on the reconstructed images has been investigated by Zwiers [26]. Figure 15 shows a schematic overview of tilt. A blood vessel is shown at an angle in the XZ-plane when compared to the XY plane of the US detector.

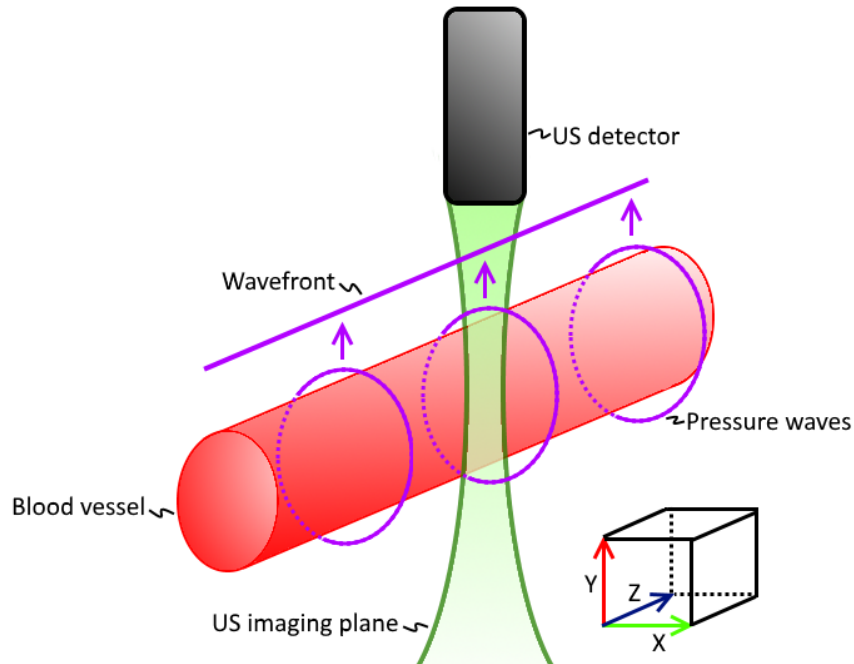


Figure 15: Schematic example of horizontal tilt. The image shows an US detector measuring in the XY-plane. It is important to note that the blood vessel is not perpendicular to the XY plane.

Tilt causes blurring in the reconstructed PA image. An example of the blurring effect is shown in Figure 16. This figure shows a schematic example of blurring on the left hand side and a phantom measurement with a horizontal tilt of 20° on the right hand side, as reported by Zwiers [26]. In this image the blood vessel appears deformed, with streaks appearing on the side that faces away from the sensor element towards the bone surface.

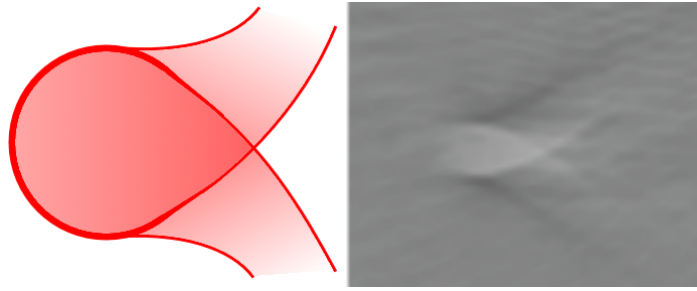


Figure 16: *Left hand side: schematic example of blurring. Right hand side: phantom measurement with a horizontal tilt of 20° , as reported by Zwiers [26].*

Although horizontal and vertical tilt of blood vessels does introduce artefacts and blurring in the final images, it was found by Zwiers that tilt is not the main source of the investigated image artefacts, as described in section 1.5. Her measurements found that acoustic reflection on surfaces such as bone plays a greater role in artefacts seen in reconstructed images. She concluded that the configuration of tissue and bone has a direct relation to the shape and size of reflection artefacts [26].

2.2 Hardware Aspects

Artefacts seen in reconstructed images can also originate from hardware aspects. One of these aspects is the shape and size of the ultrasound array used in the HTFI. The ultrasound array in the HTFI is not completely circular. It is stated in the technical report that the array is modeled to be a semi-circle with a radius of 36 mm and an active length of 107.6 mm, but there are some deviations.

Figure 17 shows a comparison between sensor elements on a perfect semi-circle with a radius of 36 mm, and the location of the real sensor elements of the 7.5 MHz array in the HTFI. The deviations of the real elements from the ideal locations are largest on the top of the semi-circle. An effect of this deviation is that signals originating from the center of the semi-circle are detected later by the elements on the top of the semi-circle than by the elements on the sides. The deviation can introduce vertical blur in the reconstructed images unless it is accounted for.

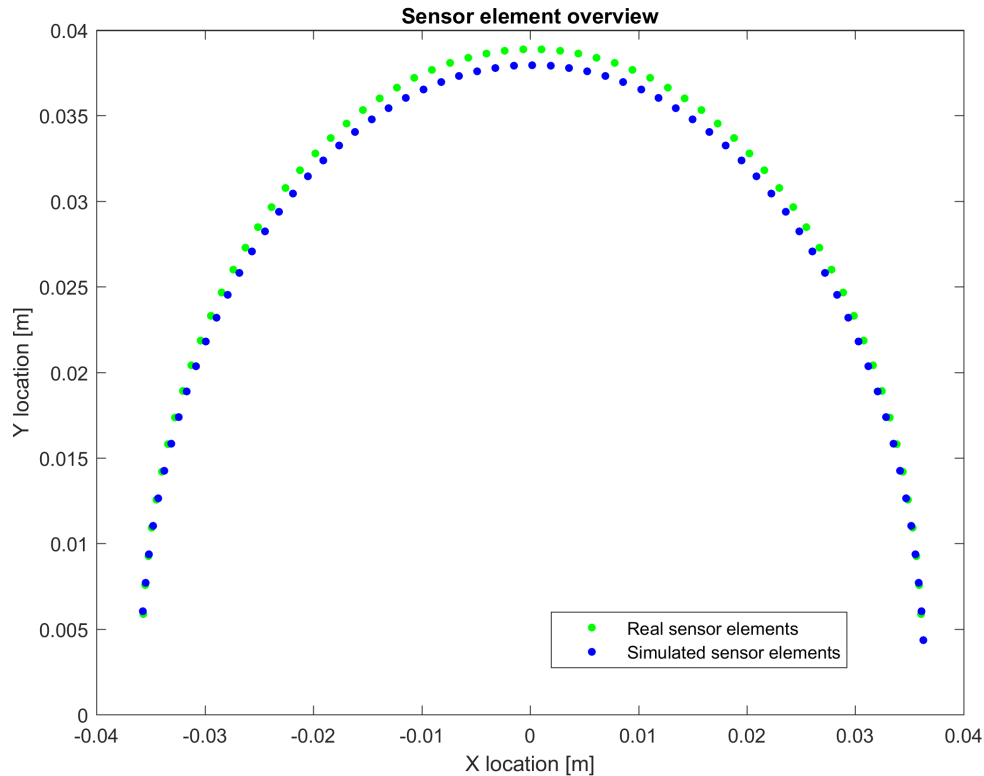


Figure 17: A comparison between sensor elements on a perfect semi-circle (blue) with a radius of 36 mm and the location of the real sensor elements (green). The deviations of the real elements from the ideal locations are largest on the top of the semi-circle.

Also worth noting that sensor element number 1 is defective and does not record signals. Although the output signal of element 1 can be removed and accounted for, it means that the US array effectively operates with 63 elements and thus does not fully cover the design specification of 172° .

2.3 Algorithm Aspects

The reconstruction algorithm can also create artefacts. This section describes two types of artefacts: single projection artefacts and speed of sound deviation artefacts.

2.3.1 Single projection

Single projection has been used during patient measurements with the HTFI. This means that multiple slices of the patients finger were imaged, without rotation of the US array to cover more angles of the same slices of the finger. This has the effect that reconstructed wave fronts on the vertical center axis overlap, resulting in a vertical intensity streak.

Figure 18 gives a schematic example of the cause for streak artefacts due to single projection. The reconstructed wave fronts from opposing sensor elements overlap in the center of the final image. This has the effect that the reconstructed intensity at the overlapping area is the sum of both wave fronts, and thus might be higher than the actual measured intensity. A vertical streak artefact can then be seen in the image as a result of this effect.

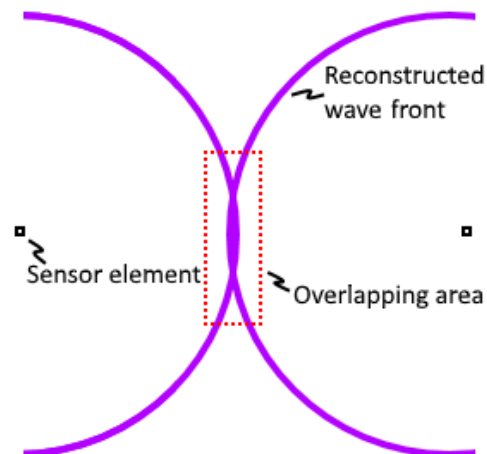


Figure 18: *Schematic example of a streak artefact due to single projection. This figure shows two sensor elements opposing each other. The reconstructed wave fronts from the sensor elements overlap in the area between the two sensor elements. The reconstructed local intensity at the overlap is a sum of both reconstructed wave fronts.*

An example of what is hypothesised to be a streak due to single projection is shown in Figure 19. This figure is from a single projection patient measurement of Vlieg [27]. Two white lines have been added by hand to the image to emphasize the overlapping of the reconstructed wave fronts. The area which is affected by overlap of the wave fronts due to single projection is highlighted on the right hand side of the image.

Simulations have been conducted on the effect and influence of single projection on the reconstructed images. The simulations and the results are described in section 3.5.

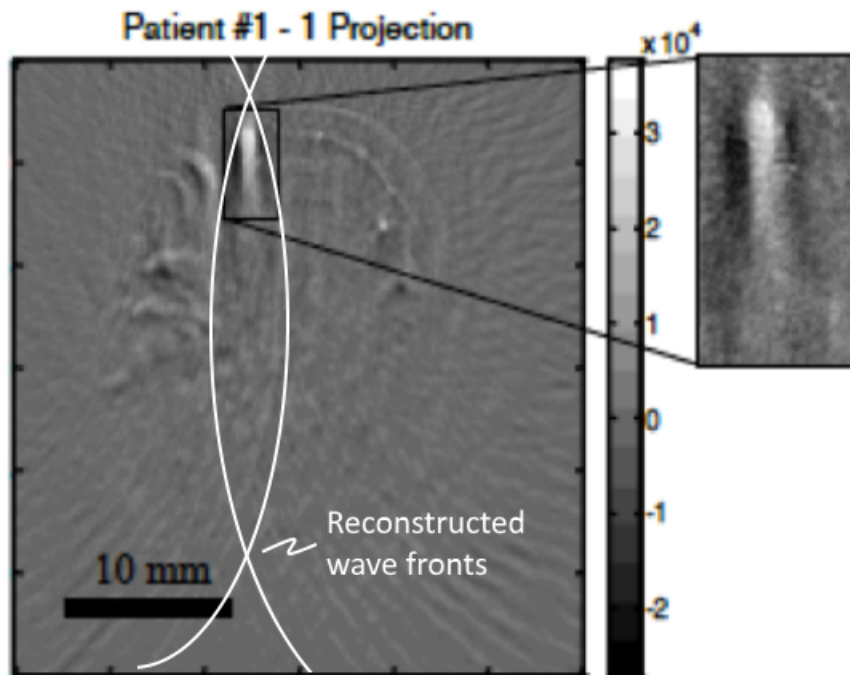


Figure 19: Example of what is hypothesised to be a streak due to single projection used during a patient measurement by Vlieg [27]. The overlapping of the reconstructed wave fronts is emphasized by the two white lines. The highlighted image on the right hand side shows the area which is affected by the overlap of the wavefronts.

2.3.2 Effect of speed of sound deviations

The speed of sound used in the reconstruction of the photoacoustic image plays a major role in the final image quality. Correct estimation of the speed of sound allows for accurate simulation of streak artefacts and acoustic reflection.

Previous work and simulations within this research have been performed with the values listed in Table 2 [26]. The values were revised and the updated values are also listed in the table [36, 37].

Table 2: *Speed of sound values used in the previous and current work. The column 'Prev. SoS.' lists the speed of sound used for different tissues in previous work. The column 'Prev. ρ ' lists the used densities in previous work. The columns 'New SoS' and 'New ρ ' list the values used in this report. The percentual difference between the new and old values is listed between brackets [36, 37].*

	Prev. SoS [m/s]	Prev. ρ [kg/m ³]	New SoS [m/s]	New ρ [kg/m ³]
Water	1482	1000	1540 (3.9%)	1000
Soft tissue	1560	1050	1560	1050
bone	2330	1386	3746(60.8%)	1975 (42.5%)

Simulations were used to investigate the origin and behaviour of the artefacts as described in section 3.3. These simulations depend on a computational grid which determines the frequency range of the simulation and the resolution of the outputted image from the simulation result. Changes with previous work on simulations in this research include that the computational grid size has been increased from 1024x1024 pixels including a perfect matching layer (PML) of 40 points to a grid size of 1440x1440 including a PML of 20 points. The PML is a layer on the boundaries of the computation grid which absorbs pressure waves at the edges of the simulation grid and prevents wrapping of pressure waves. The grid in the previous work was able to simulate frequencies up to 9 MHz, while the grid used in this work is able to simulate frequencies up to 13.16 MHz. The technical report of the used 7.5MHz array of the HTFI states that the elements can record frequencies in the range of 5-10 MHz. Using a grid which excludes the top frequencies limits the accuracy of the simulation.

Another difference in the used simulation grids is that in previous work an arbitrary power law absorption was set for the simulation grid. This means that all different tissue types in the simulation had the exact same amount of acoustic absorption. In this work, the absorption was set according to the different tissue types, which improves the accuracy of the model.

The reference speed of sound in previous work for this research was set at 1480m/s, while the reference sound speed in this work is set at 1505 m/s. It was found in labjournals that patient measurements on the HTFI were performed with a water temperature of 28.5°C. According to Del Grosso et al. [36] the speed of sound in water at a temperature of 28.5°C is \sim 1505 m/s, while the previously used 1480 m/s applies to a water temperature of 19°C.

2.4 Conclusion

From this chapter it can be concluded that the main source of the so-called streak artefacts must be found in acoustic reflection on bone surface. Single projection used during patient measurements and the overlapping of the reconstructed pressure waves in the final images has an additional effect by creating vertical intensity streak artefacts in the final images. The effects of acoustic reflection, clutter and single projection are investigated in section 3 and 4.

Chapter 3

Investigation of Clutter

Simulations were used to investigate the effect of clutter on reconstructed PA images. A description of the used simulations is provided and thereafter the results are discussed.

3.1 Introduction to Monte Carlo simulations

A 3D Monte Carlo model was used to investigate the absorption of the photons in the imaged tissue and to investigate the effectiveness of the used illumination set-up in the HTFI.

Monte Carlo simulations are commonly used to simulate a repeated process of random events, where every iteration of the simulation has a changed set of starting parameters. The final outcome of the simulation is the collection of all iterations and outputs a distribution function which covers all possible outcomes. Depending on the situation, a Monte Carlo simulation can be repeated thousands of times [38].

An overview of the utilized Monte Carlo model is shown in Figure 20. The input files contain the model parameters. The most important parameters are given below:

- Tissue model with absorption (μ_a) and scattering (μ_s) parameters per tissue.
- Number of photons to be simulated: set at 1.5 million
- Angle of illumination of the fiber relative to the skin: from 45° to 70°
- Opening angle of the fiber: 22°
- Illumination distance from the fiber to the skin: 6 cm

After the parameters and the tissue model are imported, the major cycle for the Monte Carlo simulation is initiated. The major cycle controls the launching of photons and keeps the simulation running until all requested photons are launched. The launch step then initializes the photon position and trajectory. This step will also make sure that a collimated beam is launched starting at the source location (fiber tip) towards the focus on the skin surface of the simulated finger.

After launching a photon, the photon will go through the so-called 'Hop Drop Spin Roulette' routine [39]. This routine will propagate the photon until it is absorbed, which is determined by 'roulette'. 'Hop' moves the photon with a predetermined step distance into a new voxel.

'Drop' will drop the photon weight (W) into the local voxel. Each photon is initiated with a weight value of 1 and if this value falls below the set threshold of 0.01, the photon is absorbed in the current voxel. If the photon is not absorbed in the voxel, the photon weight will be reduced as given by formula 7:

$$W_{new} = W (1 - e^{(-\mu_a s)}) \quad (7)$$

3. INVESTIGATION OF CLUTTER

With s as a random step size in centimeters given by formula 8:

$$s = -\log(x) \quad (8)$$

Where x is defined as a random number with a range between 0.1 and 1. This makes that the step size s ranges from 0.1 to 2.3 centimeters [39]..

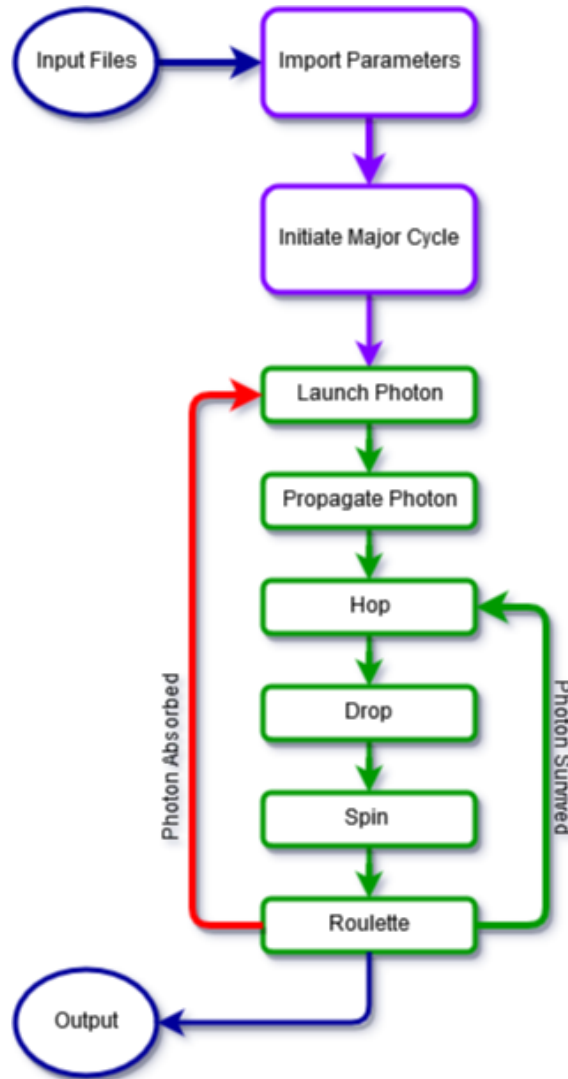


Figure 20: Schematic overview of the Monte Carlo model. The simulation starts importing model parameters from input files. After the parameters are set the major Monte Carlo cycle is initiated and this cycle continues to run until all photons are launched and simulated. The photon will go through several different steps (green) until it is absorbed. After the simulation is complete, an output is generated which contains the fluence map of the model.

The spin step scatters the photon into a new trajectory, where the new photon trajectory is determined based on the Henyey-Greenstein scattering function. The Henyey-Greenstein function is used to approximate the angular scattering dependence of single scattering events in biological tissue [40].

If the photon weight has fallen below the threshold of 0.01 the photon will be handled by the roulette routine. In the roulette routine the photon has 90% chance of being absorbed but also has a 10% chance of having its weight increased by a value of 0.1. If the photon weight is increased, the photon is not terminated and will continue to see another cycle of the 'Hop-Drop-Spin-Roulette' routine [39].

3.2 3D Modelling

The strength and quality of the Monte Carlo simulation is depending on the tissue model used. Due to the fact that the Monte Carlo simulation is run in three dimensions, the development of a 3D tissue model was required. In order to built a 3D tissue model, a 2D finger model was built first. This model is shown in Figure 21. In the model the bone is shown as green, blood vessels as red, tendons are grey and the dermis is colored pink.

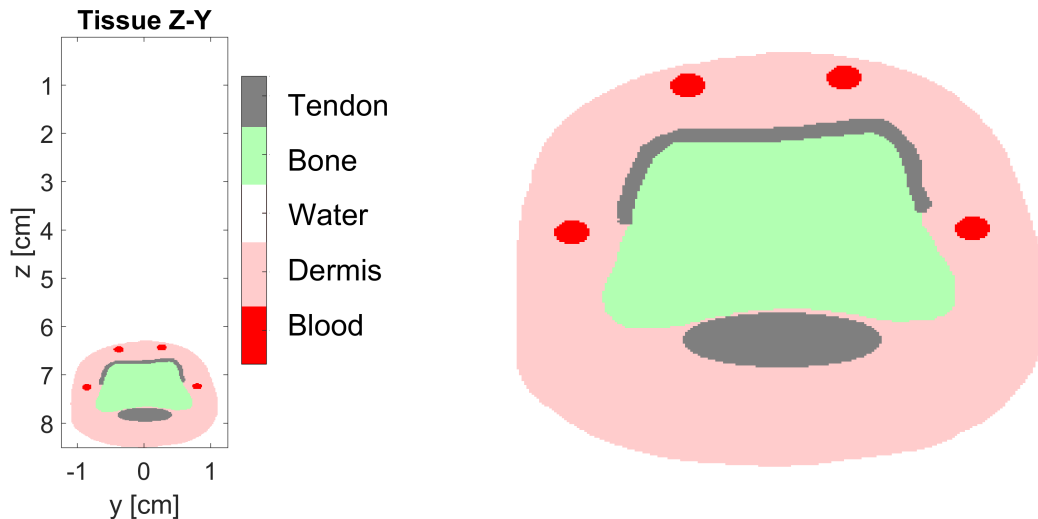


Figure 21: An enlarged overview of the two dimensional tissue model on the right hand side and the tissue model placed in the Monte Carlo model on the left hand side. The bone in the model is shown in green, blood vessels in red, tendon in grey and the dermis in pink.

The 2D image was then stacked and duplicated in the third dimension to obtain a 3D matrix from the 2D image. Figure 22 gives an illustrative example of a matrix stack, where each page consists of the columns and rows of a single 2D image. Figure 23 gives a schematic overview of the orientation of the finger tissue model in the 3D axis of the Monte Carlo model.

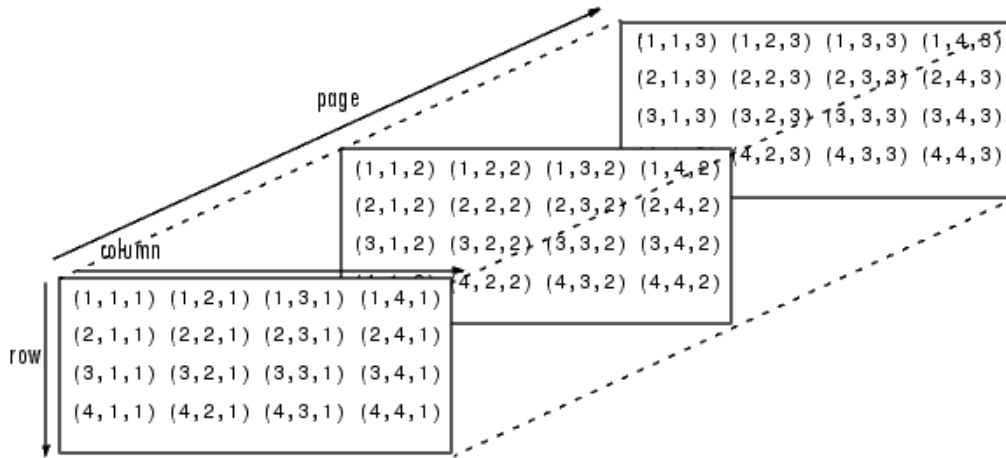


Figure 22: Illustrative example of a matrix stack, where each page consists of columns and rows and these two combined represent an image. To gain a 3D matrix from a 2D image, the 2D image is copied to all pages of the matrix.

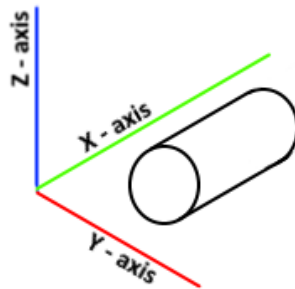


Figure 23: Schematic overview of the orientation of the finger tissue model in the coordinate frame of the Monte Carlo model.

Table 3 gives an overview of the used absorption, scattering and anisotropy values in the model. All values except those listed for bone are modeled to values listed in literature [39, 41]. The values listed for bone are arbitrarily high values, in an attempt to prevent any absorption or scattering of photons in the modeled bone. In this research it is assumed that there is no absorption of light in bone as only the absorption of photons in the blood vessels are of interest for the simulation as explained in section 3.4.

3. INVESTIGATION OF CLUTTER

Table 3: Absorption, scattering and anisotropy values as used in the Monte Carlo model. Column μ_a lists the absorption values, μ_s the scattering values and g the anisotropy. The values for bone, marked with an asterisk(*), are arbitrarily set values [39, 41].

Tissue type	μ_a	μ_s	g
Water	0.02	10	1
Dermis	0.0215	224.8	0.9
Tendon	0.0125	000	0.9
Bone	200*	200*	-1*
Blood vessel	4.3159	62.5	0.9

After all parameters as listed in Table 3 for the simulation are set, the laser beam can be projected onto the skin surface. Figure 24 shows the laser beam in the xz -plane at y is 0. This figure shows an schematic overview of the path of the laser beam for an incidence angle of 60 degrees. The different layers in the modeled tissue are visible and can be distinguished by the different colors.

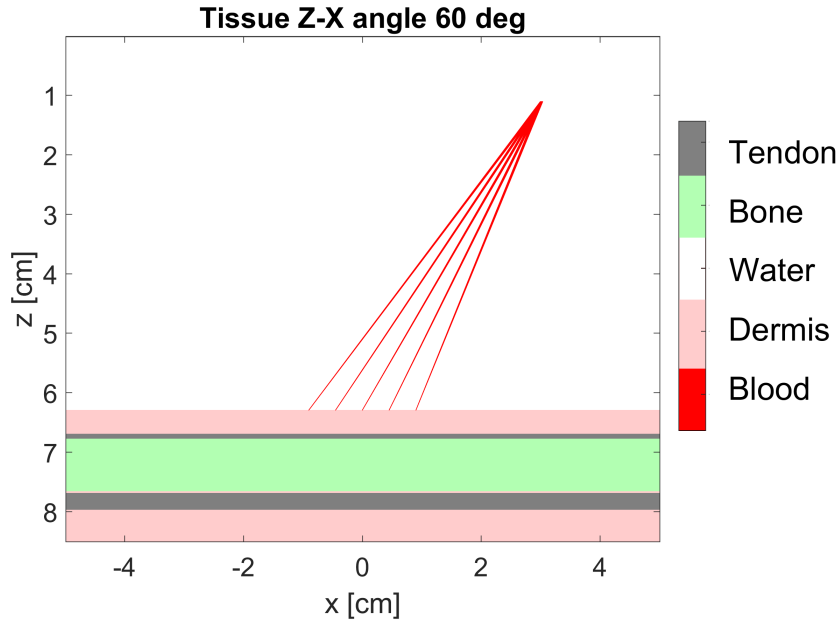


Figure 24: Schematic xz -view of the modeled tissue with the laser beam projected onto the skin with an incidence angle of the laser beam of 60 degrees. The different layers in the modeled tissue are indicated by different colors.

3.2.1 Monte Carlo Results

The simulations for the Monte Carlo experiments have been performed for 1.5 million photons, at an illumination distance of 6 cm from the skin surface, for the following incidence angles: 45, 50, 51, 55, 60, 65 and 70 degrees. An investigation on the amount of simulated photons is provided in appendix section A.

Figure 25 and Figure 26 give an overview of the fluence map (absorbed energy in the area) of the simulation for an incidence angle of 51 and 60 degrees. These angles are the illumination angles used in the HTFI. Currently 51 degrees is used, but the HTFI is also able to image fingers with an incidence illumination angle of 60 degrees. The beam path is visible as the colored prismatic cone and the area where absorption has taken place is differentiated from the background with (blue) colors. The top of the dermis layer of the tissue model is situated at z is 6.5 cm. Photons reflecting/scattering from the dermis layer and escaping into the surrounding water can be seen as the dark blue and gray background colored background.

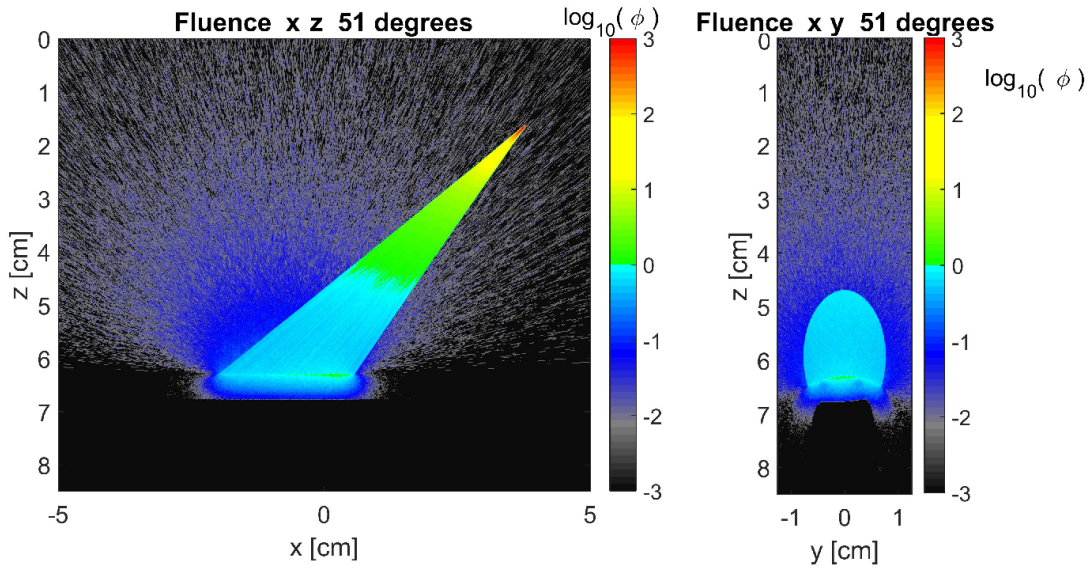


Figure 25: Overview of the fluence map of the simulation for an incidence angle of 51 degrees for 1.5 million simulated photons. The image on the left hand side shows the side view in the xz -plane at the slice y is zero. The beam path is visible as the colored prismatic cone and the area where absorption has taken place is distinguishable from the background with the different colors. The image on the right hand side shows the frontal view in the yz -plane at x is zero. A part of the beam and the absorption in the tissue model at different locations is visible. The scale bar of the figures shows the locally absorbed photons as a ratio of intensity.

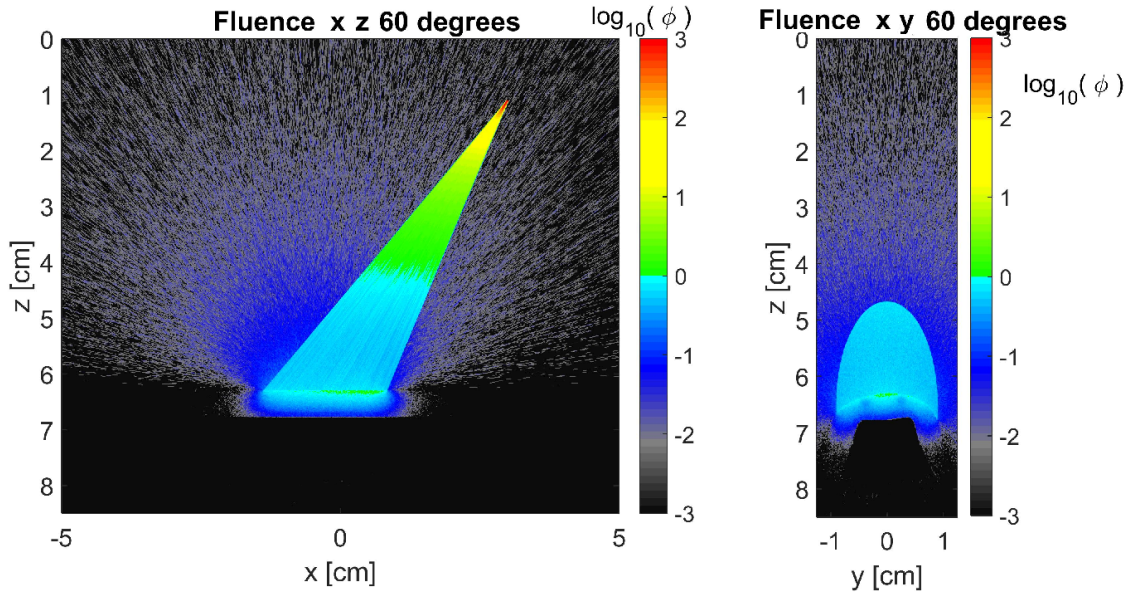


Figure 26: Overview of the fluence map of the simulation with an incidence angle of 60 degrees for 1.5 million simulated photons. The image on the left hand side shows the side view in the xz -plane at the slice y is zero. The beam path is visible as the colored prismatic cone and the area where absorption has taken place is distinguishable from the background with the different colors. The image on the right hand side shows the frontal view in the yz -plane at x is zero. A part of the beam and the absorption in the tissue model at different locations is visible. The scale bar of the figures shows the locally absorbed photons as a ratio of intensity.

Figure 27 gives an overview of the absorbed energy in the tissue model and blood vessels from the results for the illumination angle of 51 degrees. The images respectively show the full absorption from the simulation, the absorbed energy in the tissue model and the absorbed energy in the blood vessels. The absorbed energy in the blood vessels is extracted by setting all non blood vessel voxels to zero and is used as input for the out of plane clutter simulations, as described in section 3.4. Background signal can be observed in the full image, where photons have escaped into the surrounding water and a part of the laser beam is visible directly above the tissue model. The tissue model image in the center shows the higher absorption of photons in the blood vessels when compared to the surrounding tissue. The image with only the blood vessels shows that the absorption in the blood vessels closer to the beam is higher than in the blood vessels on the lower sides of the tissue model.

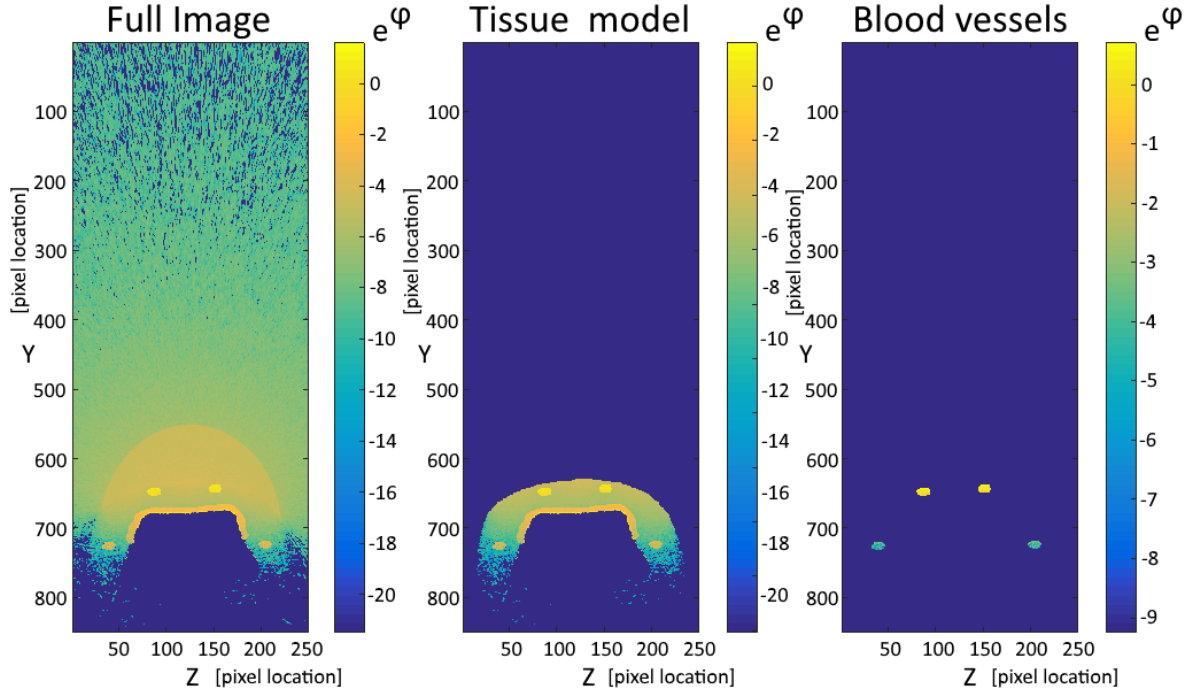


Figure 27: Overview of the absorbed and extracted energy in the tissue model and blood vessels from the results with the illumination angle of 51 degrees. All images shown in this figure are displayed at the slice position x is -1 cm when compared to Figure 25. The full absorption is shown on the left hand side. The absorbed energy in the tissue model is shown in the middle and the absorbed energy in the blood vessels is shown on the right hand side. The scalebar shows the absorbed photons as a ratio of intensity. The intensity is given as e^ϕ , with ϕ as the (negative) scalebar value.

Figure 28 shows an overview of the absorbed energy in the modeled tissue for different illumination angles of the fibers. Note the broad area under the curve for the illumination angle of 45°. This angle can illuminate a large area, but also results in the lowest absorbed energy. The curves of 60, 65 and 70 degrees show minor differences in illumination area and absorbed energy. The graph shows that the current used illumination setup of 51 degrees in the HTFI is able to illuminate a larger area on the finger, but results in a lower overall absorbed energy than the illumination setup of 60 degrees.

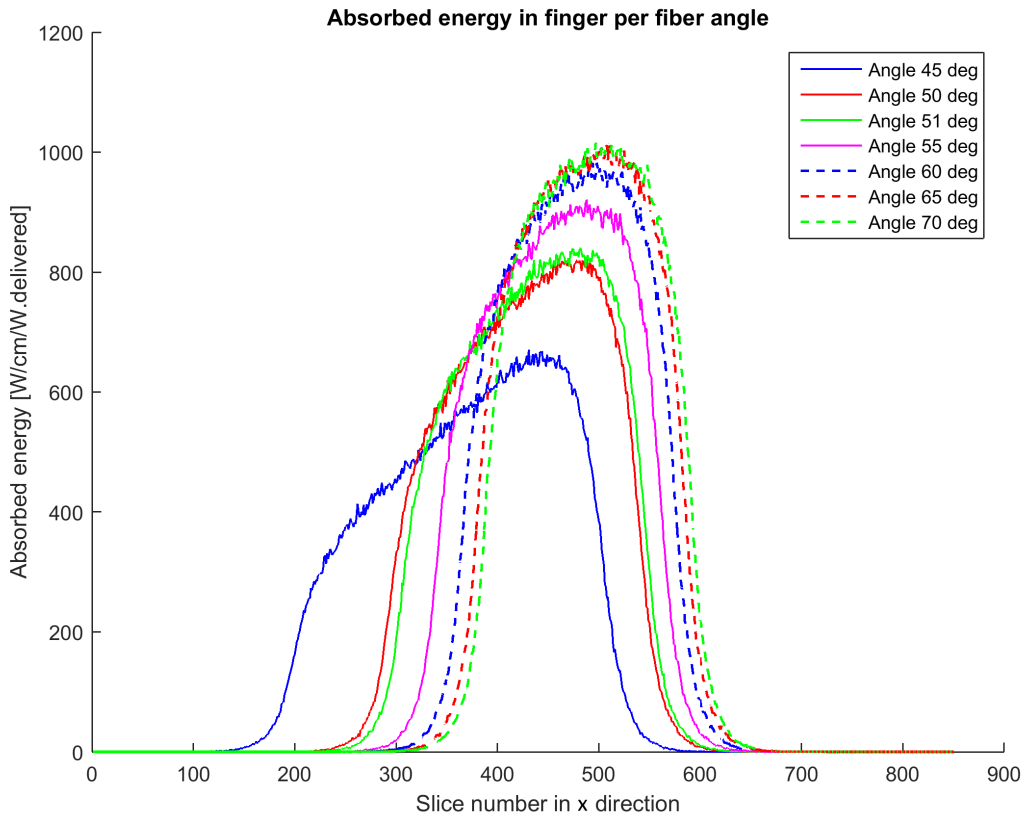


Figure 28: Overview of the absorbed energy in the modeled tissue for different illumination angles of the fibers. Worth noticing is the broad area under the curve for the illumination angle of 45°. This angle can illuminate a large area, but also results in the lowest absorbed energy. The curves of 60, 65 and 70 degrees show minor differences in illumination area and absorbed energy when compared to each other.

The results from the Monte Carlo simulations, such as the 3D fluence matrix, are used in photoacoustic simulations. With these data, the effect out of plane clutter was studied. The implementation of k-Wave is described in section 3.3. The results from the out of plane clutter simulations are provided in section 3.4.

3.3 Implementation in k-Wave

K-Wave is a software package that can be used in combination with Matlab to simulate and investigate the behaviour of photoacoustic signals [24]. This software package was used in an attempt to simulate the observed streak artefacts in the results of the patient measurements and investigate the behavior of the artefacts in different scenarios. These scenarios include out of plane clutter as described in section 2.1.1 and acoustic reflection, as described in section 2.1.2. To simulate these scenarios, the tissue model described in section 3.2 was implemented in k-Wave. The parameters of this tissue model were used in combination with the fluence map (resulting from the Monte Carlo simulation), to obtain the absorbed energy in the tissue. The absorbed energy is given by equation 9.

$$Ea = F(x, y, z) \mu_a(x, y, z) \quad (9)$$

With Ea as the absorbed energy in the tissue, F as the fluence (J/cm^3) and μ_a (cm^{-1}) as the absorption coefficient of the tissue. It is important to note that both the fluence map and the absorption coefficient are given as an 3D matrix, as every tissue type has a different absorption value.

From the absorbed energy it is then possible to calculate the initial pressure. The initial pressure is used as input in the k-Wave model and can be calculated by multiplying the absorbed energy in the tissue with the Grüneisen coefficient (denoted by the Greek capital letter gamma, Γ) of the tissue. The relation to calculate the initial pressure is given in equation 10 and previously discussed in section 1.2.

$$p_0 = \Gamma Ea = \left(\frac{\beta c_s^2}{c_p}\right) Ea \quad (10)$$

With p_0 as the initial pressure, Γ as the Grüneisen coefficient, β as the thermal expansion coefficient, c_s as the speed of sound in the tissue and c_p as the thermal heat capacity of the tissue. This relation shows that the Grüneisen coefficient depends on several parameters of the tissue, and thus differs with varying tissue types.

An overview of the acoustic properties used in the k-Wave model is given in Table 4. What stands out is that the tissue model for the tendon, as shown in the Monte Carlo simulations, is left out. The tendon was set as dermis in the k-Wave simulation to reduce complexity of the tissue model. The values for the speed of sound, acoustic absorption coefficient, tissue density and thermal heat capacity are listed. The values for the acoustic absorption coefficient in the k-Wave model have the limitation that they have to be between 1 and 7, and must be rounded to the nearest integer. This resulted in the values as listed in the table. The value for β as the thermal expansion coefficient is set as the volumetric expansion coefficient of water at 20°C, which is equal to $2.07e^{-4}/^\circ C$ [42]. As there is no absorption of photons in the modeled bone, the value for β for bone is arbitrary set to 1.

3. INVESTIGATION OF CLUTTER

Table 4: Overview of the acoustic properties used in the *k*-Wave model. With *SoS* as speed of sound, α (alpha) as the acoustic absorption coefficient, ρ (rho) as the tissue density and c_p as the thermal heat capacity [36, 37].

Tissue	SoS [m/s]	α [dB/MHz/cm]	ρ [kg/m ³]	c_p [J/g°C]
Bone	3476	7	1975	1.3
Blood	1616	1	1066	3.84
Dermis	1560	1	1050	3.39
Water	1505	1	1000	4.18

Figure 29 provides a schematic overview of the implementation of the model in *k*-Wave from the results of the Monte Carlo simulation. This figure shows the input files and parameters in the blue circle as initial starting point for the Monte Carlo simulation. The Monte Carlo simulation outputs the fluence map, from which the absorbed energy in the finger can be calculated. The absorbed energy is used as initial pressure in the *k*-Wave simulation. The absorbed energy is used as initial pressure in the *k*-Wave simulation.

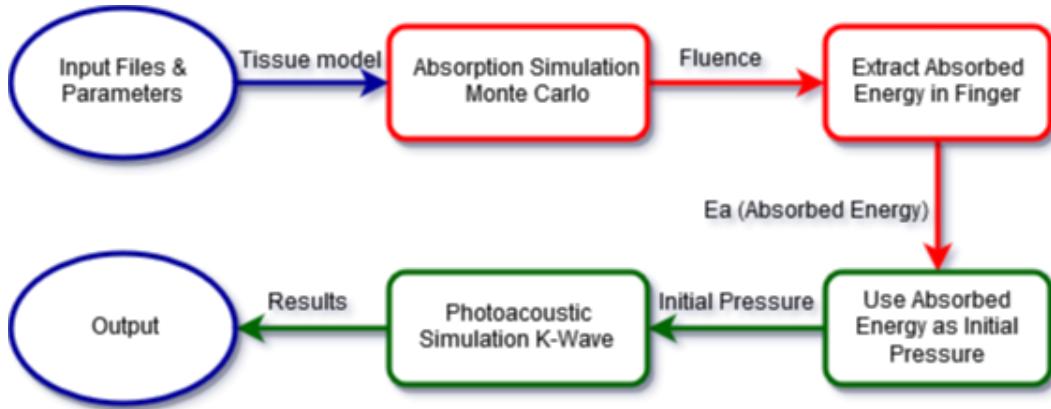


Figure 29: Overview of the implementation of the model in *k*-Wave from the results of the Monte Carlo simulation.

3.3.1 *k*-Wave Technical Properties

All simulations were performed for 35 μ s in 3501 time steps with a time step of 10 ns. The effective grid size of the simulations is 1400x1400 points with a maximum supported frequency of 13.16 MHz. The grid is set to measure 8 cm in width and height, which makes that the voxels have a size of $5.7e^{-5}$ m. The grid is surrounded by a perfect matching layer (PML) of 20 points which absorbs pressure waves at the boundary of the grid and prevents wrapping of the pressure waves. The full grid measures 1440x1440 points with the addition of the PML.

The *k*-Wave simulation consists of two parts. First a forward simulation is performed, in which the photoacoustic signals originating from the initial pressure are recorded by the sensor elements. The second part of the simulation contains the reconstruction of the recorded signals. The recorded sensor data is filtered after the forward simulation is complete. The filtering is performed with a Gaussian filter with a center frequency of 7.5 MHz in order to make the simulation match with the sensor elements of the HTFI as close as possible. An overview of

the filter and filtered signal is given in Figure 30. The original signal is shown in black in this figure. The Gaussian filter is shown as the blue bell curve and the remaining signal is shown in red. An overview of the effect of filtering is given in appendix section B.

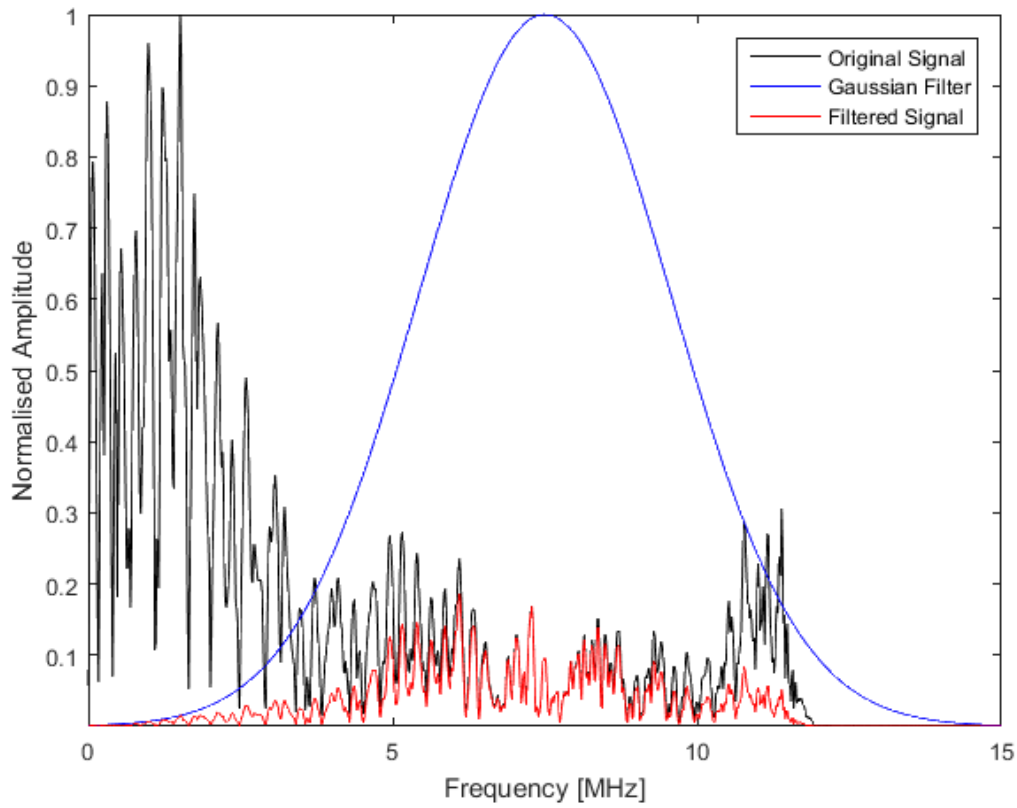


Figure 30: An overview of the applied Gaussian filter on the recorded sensor data. The original signal is shown in black. The Gaussian filter is shown as the blue bell curve, with the peak at 7.5 MHz. The red signal is the remaining signal after filtering.

3.4 Simulation of Monte Carlo Out of Plane data

Out of plane clutter was simulated in k-Wave to investigate the effect on the reconstructed photoacoustic images. The principle of out of plane clutter is described in section 2.1.1. To investigate out of plane clutter, a 3D simulation was built in k-Wave based on the data resulting from the Monte Carlo simulations as described in section 3.2.1. The out of plane clutter simulation makes use of the same principles as described in section 3.3, with the adjustments that the dimension of the 3D matrix measures 200x200x125 voxels, with a voxel size of $4e^{-4}$ m. This limit was set due to limitations in available computational memory. The grid supports frequencies up to 1.88Mhz.

Figure 31 provides a frontal view of the setup used for the 3D out of plane clutter simulations. The image shows the ultrasound array elements in red and the tissue model in the center of the image. The initial pressure, which in this model is only initiated from the blood vessels, is extracted from the Monte Carlo results and matched to the tissue model in this simulation. An example of the extracted energy from the blood vessels is shown in Figure 27 on the right hand side.

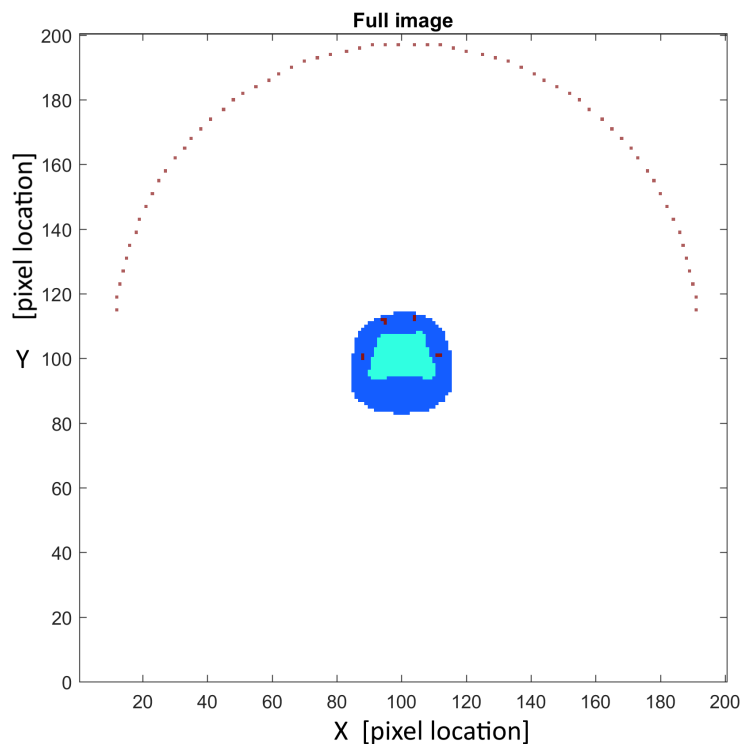


Figure 31: *The image shows the ultrasound array elements in red and the tissue model in the center of the image. The tissue model consists of bone (light blue), dermis (dark blue) and blood vessels (red).*

The simulation described in this section is performed for four different cases. An overview of the different simulation cases is given in Figure 32 and provided below:

- A: full simulation, with the blood vessels of all slices contributing to the photoacoustic signal.
- B: single slice simulation, directly beneath the US array. Only the blood vessels in this slice emit the initial pressure.
- C: simulation with slices at the far edges and in the center of the 3D matrix. Only the blood vessels in the shown slices emit the initial pressure.
- D: simulation with only a slice at the far edge at Z is 1. Only the blood vessels in this slice emit the initial pressure.

It is important to note that the tissue model as provided in Figure 31 is present in all slices for all performed simulations, but that the slices from which the initial pressure is simulated are the only ones shown in Figure 32 for illustrative purposes.

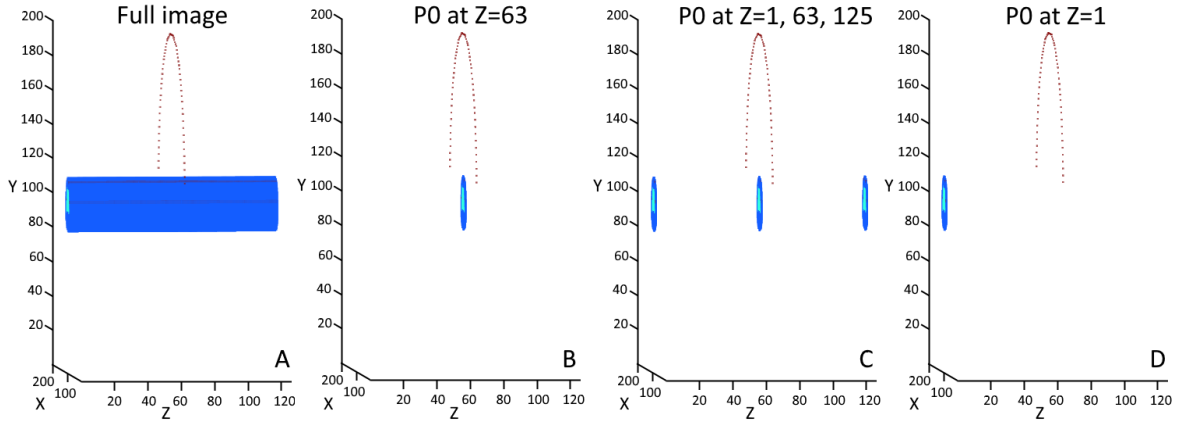


Figure 32: Overview of the different simulation cases for out of plane clutter. Image (A) shows the full image simulation, in which the blood vessels of all slices contribute to the initial pressure. Image (B) shows the single slice simulation in which only the blood vessels in the center slice emit the initial pressure. Image (C) shows the simulation where only the blood vessels from the center and edge slices contribute to the initial pressure. Image (D) shows the simulation with only blood vessels from slice Z is 1.

Figure 33 shows the results from the simulations as provided in Figure 32. Image (A) and image (B) seem to show similar results, with the note that the intensity of image (B) is a factor 10 lower than image (A). These two images show two reconstructed blood vessels as the negative (black) dots. Directly beneath these reconstructed blood vessels are small positive streaks visible, which are assumed to result from acoustic reflection on the bone in the tissue model. Image (C) has a similar result as image (B), with the addition of reconstructed pressure waves from the far planes. These reconstructed pressure waves from the far plane are the only results observed in image (D). It stands out that the overall intensity of image (D) is a factor 10^{-3} lower than image (A).

3. INVESTIGATION OF CLUTTER

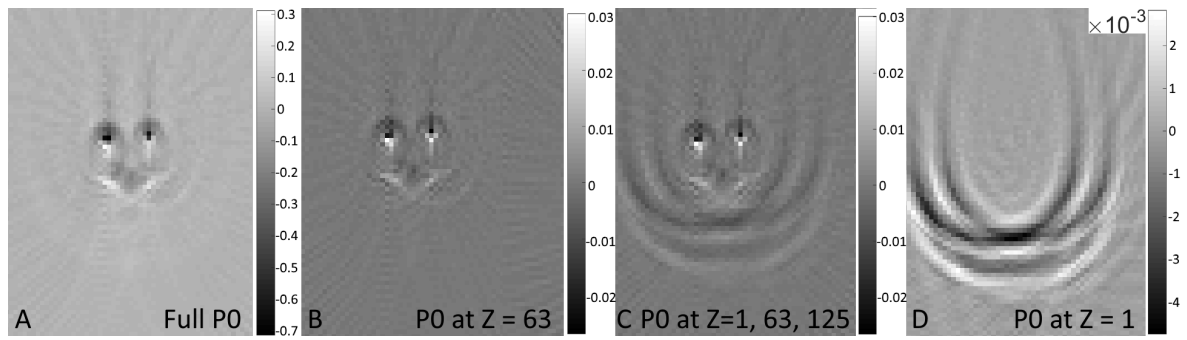


Figure 33: Overview of the results from the simulations as shown in Figure 32. (A): Result for the full simulation. (B): Result for the single slice simulation, directly beneath the US array. (C): Result for slices at the far edges and center of the 3D matrix. (D): Result for the single slice at the far edge.

3.5 Simulation of single projection

Single projection as used during the patient measurements can cause vertical intensity streak artefacts as described in section 2.3.1. This section aims to provide more insight in the effect of single projection and the influence of a strong photoacoustic source in the overlapping area of the reconstructed pressure waves. The simulations are set-up in the same manner as described in section 3.3, with the adjustment that the 2D grid size measures 640x640 voxels including a PML of 20 pixels and the grid has a voxel size of $1.33e^{-4}$ m. The grid has a supported frequency of 5.77MHz.

The simulation was performed for nine different scenarios, in which the blood vessel was placed in such way that all possible x-y pixels locations at 200, 300 and 400 were covered (e.g. $[x\ 200, y\ 200]$ and $[x\ 400, y\ 300]$). The bone was placed directly beneath the blood vessel, of which an example is provided in Figure 34. The results from the simulations are given in Figure 35. Image (A) in this figure shows the scale bar in both mm and pixel values. The images are obtained with the use of the time reversal algorithm in k-Wave.

It stands out that the reconstructed blood vessels are distinguishable in all images as the dark red areas. Directly beneath the reconstructed blood vessel is a negative (blue) area visible. When observing images (D) to (F) an overlap of the reconstructed waves can be observed as the yellow area directly above the reconstructed blood vessel. This has the effect that a vertical intensity streak artefact appears starting from the reconstructed blood vessel and going upwards in the image, following the contours of the reconstructed wave fronts. This effect is also visible on the lower side of the reconstructed blood vessels, were directly next to the negative blue area a higher intensity in yellow is shown.

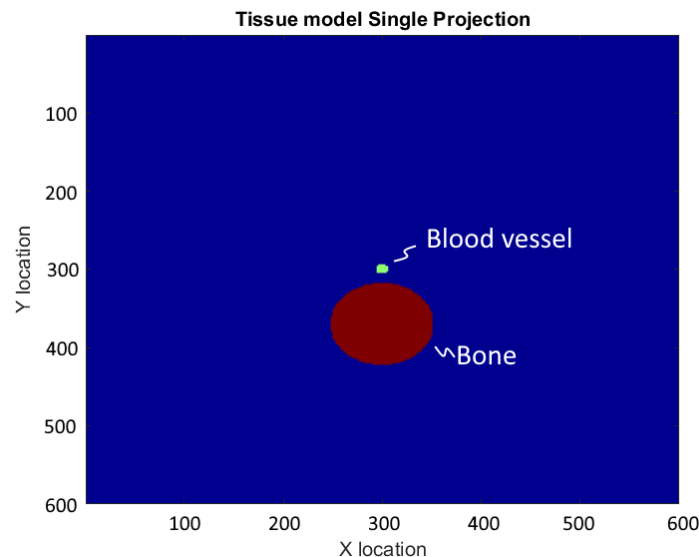


Figure 34: Overview of the single projection setup. The figure shows the water background, the bone and blood vessel. The blood vessel is used as the source for the initial pressure. The example shown in this figure is the simulation setup for image (E) of Figure 35.

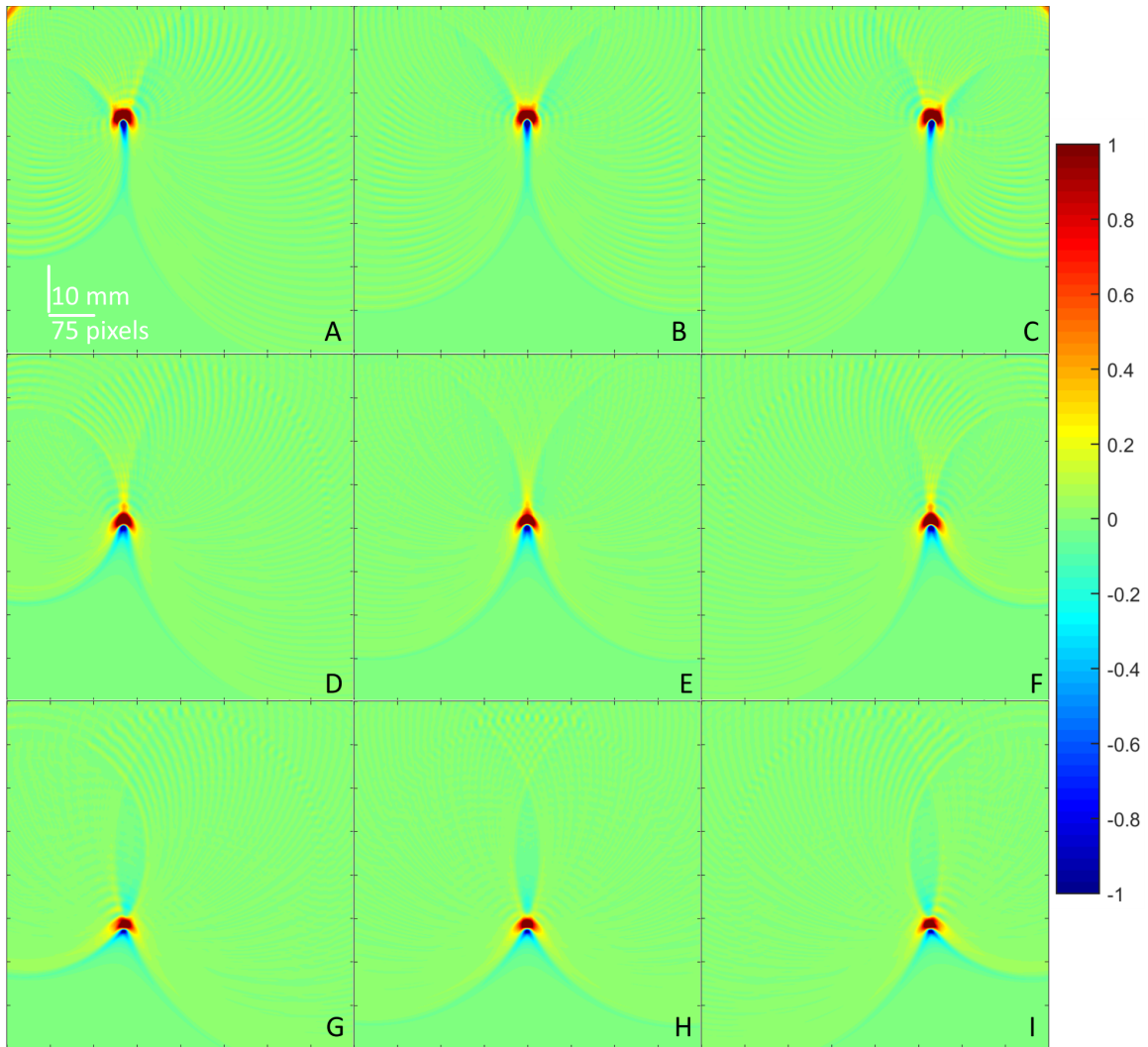


Figure 35: Overview of the single projection results obtained with the time reversal algorithm in k -Wave. Image (A) shows the scale bar in both mm and pixel values. When observing images (D) to (F) an overlap of the reconstructed waves is visible directly above the reconstructed blood vessel. In all images the reconstructed blood vessel is visible in red with directly beneath the blood vessel a negative (blue) area. The reconstructed wave fronts are shown in yellow.

3.6 Discussion

The Monte Carlo simulation has been performed with 1.5 million photons. The amount of photons simulated is just a fraction of the amount of photons which are irradiated onto the tissues in the HTFI setup. Although the amount of photons is significantly lower in the Monte Carlo simulation, it is assumed that the result from the simulation is relevant, as the ratio and distribution of absorbed photons in the tissue would remain equal with a higher number of simulated photons.

The tissue model of the Monte Carlo model does contain tendon, but the tendon was set as dermis during the importing of the Monte Carlo result into k-Wave. This choice was made in order to reduce the complexity of the model in k-Wave. It is assumed that the conversion from tendon to the dermis and the arbitrary set optical values for the bone (as described in section 3.2) have no influence on the final k-Wave result, as only the fluence map of the blood vessels (see Figure 27, right hand side) was used in the k-Wave simulation.

Information was lost by resizing the 3D fluence matrix from the Monte Carlo result to the k-Wave model. Importing the original size of the 3D fluence matrix was not possible due to the large size and limitations in computational memory in k-Wave. Resizing was performed with a nearest-neighbor approach to maintain sharp edges in the tissue model and prevent blurring and overlapping of different tissues.

As described for the out of plane clutter simulation in section 3.4, the simulation is performed in a grid which supports frequencies up to 1.88MHz due to computational limitations. It is important to note that the used sensor elements in the k-Wave simulation have an omnidirectional sensitivity. At first it was assumed that the simulation was performed with set directionality as implemented in the algorithm, but these parameters are not supported and thus not exported to the external C++ function of k-Wave which is used to perform the 3D simulation. A work around suggested in the examples of the k-Wave documentation [43] states that a large, single-aperture element can be simulated by combining multiple smaller elements, but this approach did not result in a difference in the final simulation results.

Still, it is assumed that out of plane clutter has no significant influence on the reconstructed images. By comparing the simulation result from the full simulation of Figure 33 with the result from initial pressure at z is 63, no significant difference in the images can be observed, apart from the difference in intensity scale. Another aspect to bear in mind is the size of the single detector elements, as stated in section 1.4. The sensor elements have a relatively small width when compared with the detector element length, which on itself, already introduces natural directional sensitivity of the elements. The final aspect is that the out of plane clutter signal has a signal loss of 10^{-3} , so it is assumed that out of plane clutter signal does not play a significant role in the final PA images.

The tissue model used in the single projection simulations used an arbitrary tissue model with only a single blood vessel and a round bone shape. This model does not match the finger model as described and was solely used to simplify the simulations. The results presented in Figure 35 show that for every location of the acoustic source vertical intensity streak artefacts can be observed. These artefacts appear both above and under the reconstructed blood ves-

sel. It stands out that the result in image (E) which is located in the center of the US array, has the vertical streak artefact with the highest intensity when compared to the other images.

3.7 Conclusion

From the simulations it can be concluded that out of plane clutter has no significant influence on the image quality of the final reconstructed photoacoustic images. This means that out of plane clutter is not the source of the investigated artefacts. It was found that single projection used during patient measurements does have a significant influence on the artefacts seen in the reconstructed photoacoustic images. From this chapter it can be concluded that the source of the investigated artefacts must be found with acoustic reflection and the combination of single projection.

Chapter 4

Investigation of Acoustic Reflection

This chapter describes the performed simulations used to investigate the effect of acoustic reflection on the reconstructed photoacoustic images. Simulations have been performed with numerical phantoms and patient data. The results are provided and discussed in this chapter.

4.1 Simulation of numerical phantoms

Acoustic reflection and its theory is previously discussed in section 2.1.2. In order to gain more insight in the effect of acoustic reflection and the influence of the shape and size of the bone in the finger, numerical simulations were performed. These simulations were built upon arbitrary shapes of bone in digital two-dimensional finger phantoms.

Figure 36 provides an overview of used numerical phantoms in the simulations. The simulations were performed for four different numerical phantoms, namely: (A) no bone and thus only dermis and water, (B) a circular bone shape, (C) a square bone shape and (D) a triangular bone shape. The acoustic properties were modeled to the values as listed in Table 4 of section 3.3. The simulations were performed with the settings and filtering as mentioned in section 3.3. The results from the simulations are given in Figure 37.

From the results it can be observed that the shape of the bone plays a significant role in the seen streak artefacts in the images. The reconstructed blood vessels are shown as the five black dots towards the top of the image. Directly beneath the reconstructed blood vessels are white intensity streaks visible which appear perpendicular to the surface of the bone in the phantoms. A reflection of the original blood vessel is reconstructed inside the bone of the phantoms. These reflections can be observed as the black dots in image (C) and (D) towards the center of the images. From these results, it can be concluded that the shape of the bone has a direct relation with the seen streak artefacts in the patient images.

4. INVESTIGATION OF ACOUSTIC REFLECTION

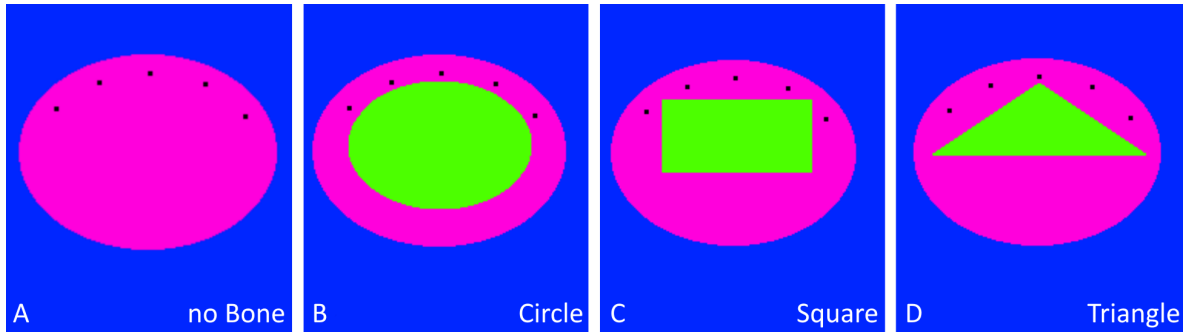


Figure 36: Numerical phantoms used in the simulation. *A:* Simulation without bone, only dermis and water. *B:* Simulation with a circular bone shape. *C:* Square bone shape. *D:* Triangular bone shape. The five small black dots are simulated locations of blood vessels and used as the starting location for the initial pressure.

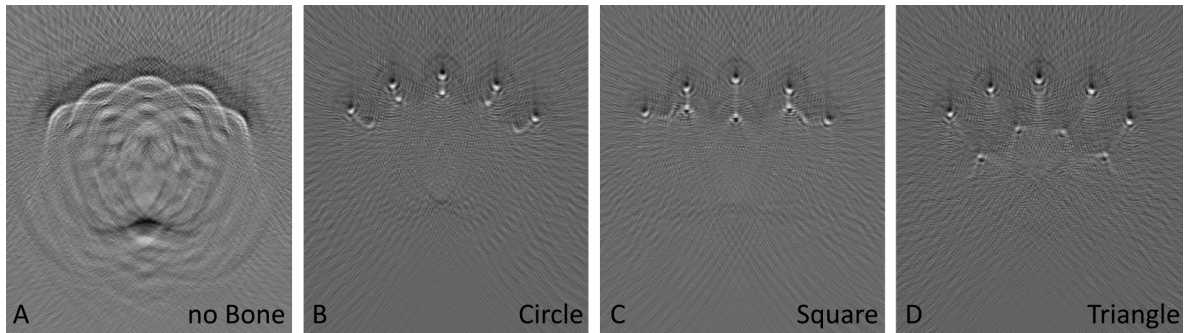


Figure 37: Results from the numerical phantoms. *A:* Result from the simulation without bone, only dermis and water. *B:* Result from the circular bone shape. *C:* Result from the square bone shape. *D:* Result from the triangular bone shape.

4.2 Simulation of patient data

As a final experiment, patient measurements were simulated in k-Wave to investigate the streak artefacts. The k-Wave settings as described in section 3.3 were used. The results from the k-Wave simulations described in this section were then compared with the real patient data. The anatomy of the patients bone, dermis and blood vessels was mimicked from the patients ultrasound and photoacoustic data and used in the simulation.

4.2.1 Simulation of patient case #1

Figure 38 provides an overview of actual patient data, measured by Zwiers [26]. The image on the left hand side shows the photoacoustic image. The ultrasound image is shown in the center and the image on the right hand side shows the ultrasound/photoacoustic overlay, where the blood vessels in the finger are shown in red.

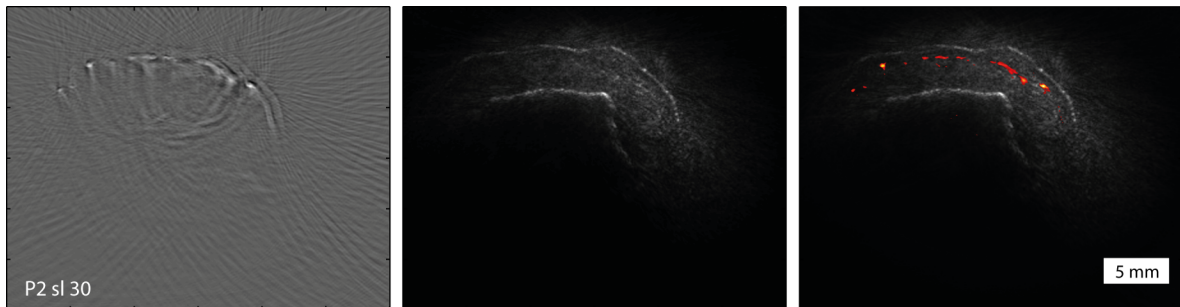


Figure 38: Results from Zwiers [26]. The image on the left hand side shows the photoacoustic image. The ultrasound image is shown in the center and the image on the right hand side shows the ultrasound/photoacoustic overlay.

It is possible to trace the outline of the patients bone, blood vessels and dermis with the help of the ultrasound/photoacoustic overlay image. These outlines were used to built a tissue model of the patients finger. This tissue model was then used with a forward simulation in k-Wave. An overlay of the tissue model used in k-Wave and the original image is given in Figure 39. Every tissue type has a different speed of sound, attenuation coefficient and density. These values influence the propagation of the pressure waves and are thus important parameters for the tissue model. These values for the different tissue types are implemented in the k-Wave simulation and are listed in Table 4 of section 3.3.

The blood vessels shown in the ultrasound/photoacoustic overlay image from Figure 38 are used as the initial pressure in the simulation. The local difference in intensity of the blood vessels as seen in Figure 39 is also implemented in the k-Wave simulation. This difference in intensity between blood vessels is caused by a difference in the local fluence, the absorbed energy in the blood vessel. This means that blood vessels with a higher intensity in the ultrasound/photoacoustic image also have a higher initial pressure in the simulation. The results of the simulation after performing the reconstruction with the time-reversal algorithm are given in Figure 40. The blood vessels are displayed as the yellow dots around the height of y is -7 mm. Directly above the reconstructed blood vessels is a negative (blue) area visible. Below the reconstructed blood vessels are streak artefacts visible as the yellow streaks which appear to meander towards the center of the bone.

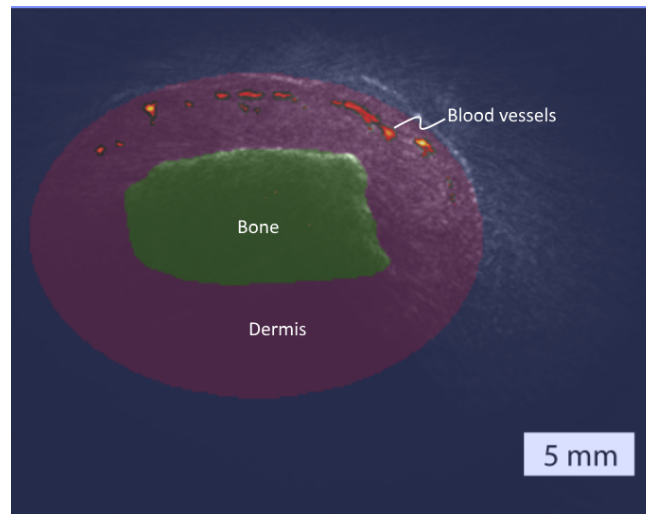


Figure 39: *Overlay of the original ultrasound/photoacoustic image and the tissue model. The outline of the bone (green), blood vessels (red) and dermis (pink) were used to build the tissue model of the patients finger.*

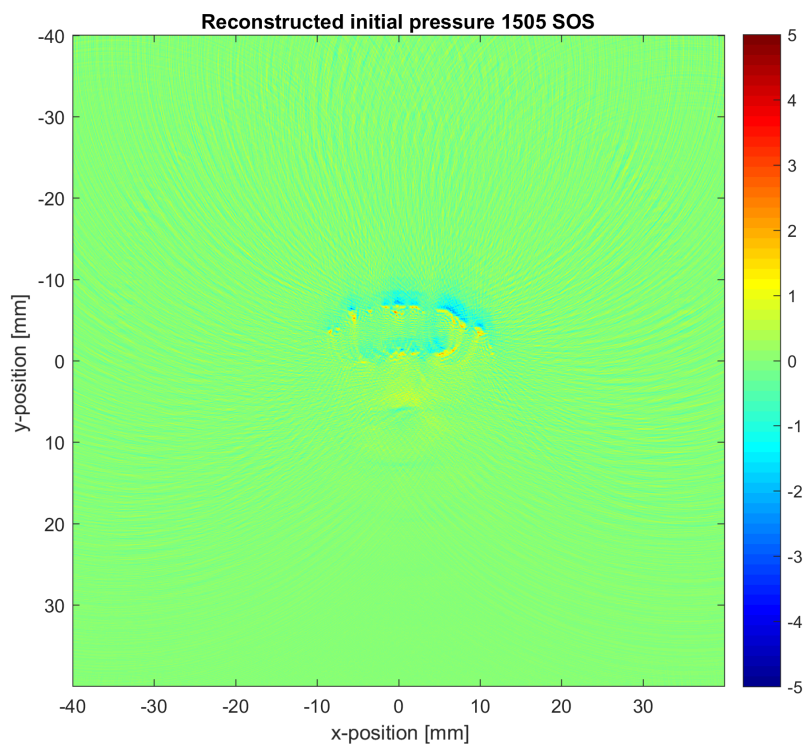


Figure 40: *Reconstructed result from the k-Wave simulation performed with time reversal. The reconstructed blood vessels are visible as the yellow dots around the height of y is -7 mm. Yellow streak artefacts can be observed meandering from the blood vessels towards the center of the bone.*

A cropped version of the result of Figure 40 is given in Figure 41 on the left hand side, which allows for a better observation of the small details in the resulting image. The image on the right hand side of this figure shows the original photoacoustic image from the patients data.

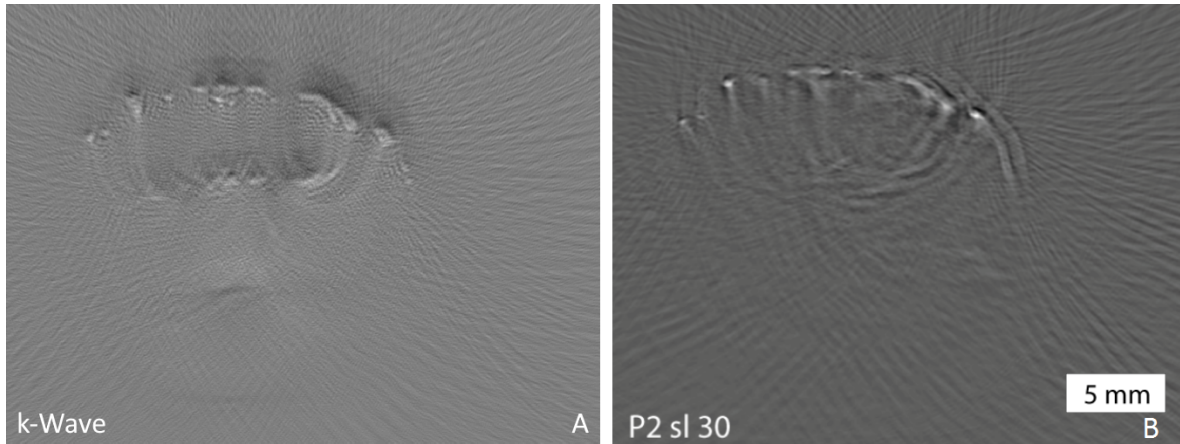


Figure 41: A cropped image of the result from the *k*-Wave simulation is shown on the left hand side (A). The original result from the patients measurement is shown on the right hand side (B).

Figure 42 shows two overlays of the original photoacoustic image from the patient and the result from the simulation. The image on the left hand side (A) shows a blend of 50% of both images, the image on the right hand side shows a blend of 30% for the simulation result and 70% for the patients image. The result from the simulation is colorized to make comparison between both images possible.

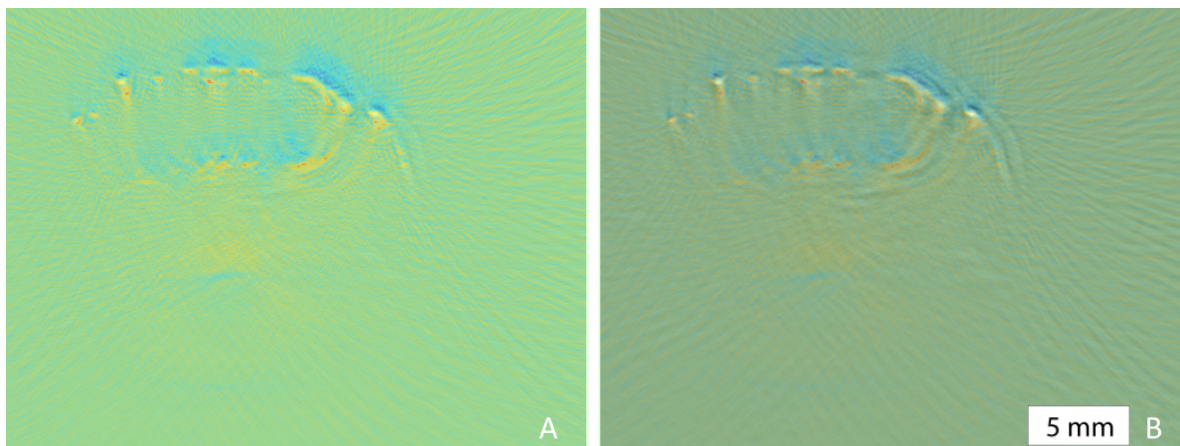


Figure 42: Two overlays of the original photoacoustic image from the patient and the result from the simulation. The image on the left hand side (A) shows a blend of 50%, the image on the right hand side shows a blend of 30% of the simulation result and 70% of the patients image.

4. INVESTIGATION OF ACOUSTIC REFLECTION

The simulations were also performed for different combinations of tissue types to investigate the effect of the reflection of the pressure waves on bone. This was done by removing certain tissue types from the simulation. For example, a simulation was run with only water, in which the bone and dermis were removed from the tissue model. For the second combination, water with dermis, the bone was removed and the area of the bone set as dermis. In the last combination, water with bone, the dermis was removed and set as water. An overview of these simulation settings is shown in Figure 43. This figure shows the different tissue type settings for which the simulations were performed. Note that in all simulations, the settings for the blood vessels and thus the initial pressure, were unchanged.

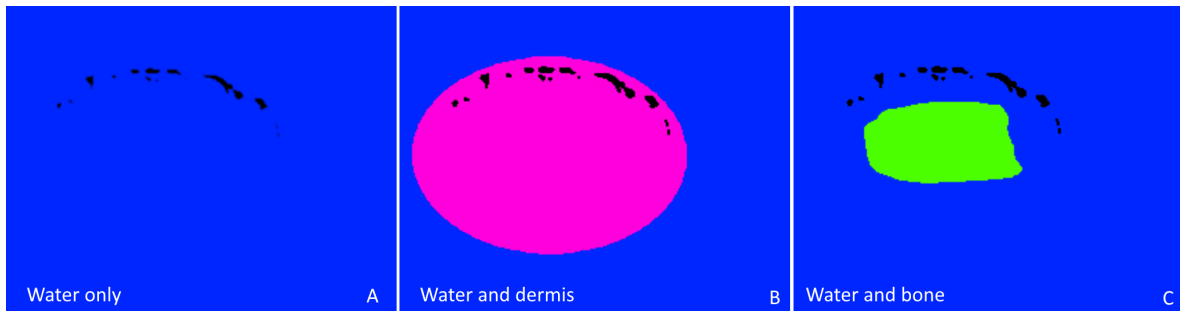


Figure 43: *The different tissue type settings for which the simulations were performed. Image (A) shows the setup with only water. Image (B) shows the setup with water and dermis. Image (C) shows the setup with water and bone.*

The results from the simulations with different tissue combinations as shown in Figure 43 are given in Figure 44. The reconstructed blood vessels are shown as the red areas in image (A) and (B). Directly above the blood vessels there is a negative (blue) area visible. Some small vertical streak artefacts can be observed directly beneath the blood vessels in image (B). When observing the result for the simulation with water and bone, it stands out that the characteristic streak artefacts seem to appear again. These streak artefacts seem similar to the streak artefacts as observed in Figure 40.

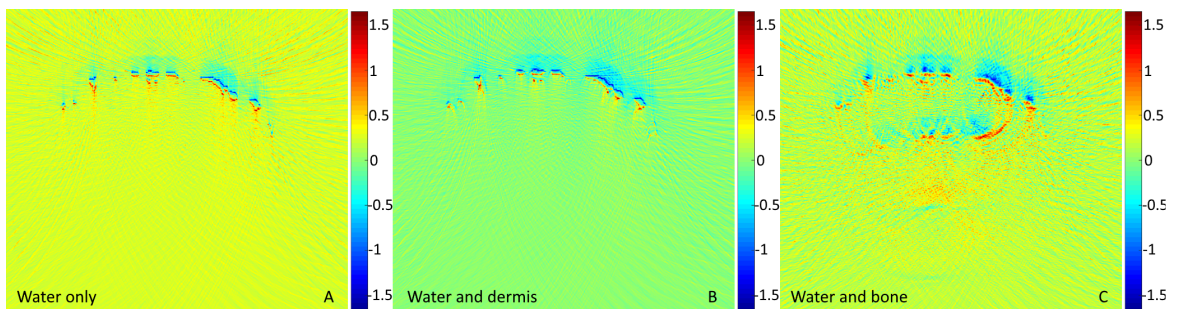


Figure 44: *Results from the simulations with different tissue combinations as shown in Figure 43. Image (A) shows the result with only water. The blood vessels are shown as the red areas. Image (B) shows the result for the simulation with water and dermis. Image (C) shows the result for the simulation with water and bone.*

4.2.2 Simulation of patient case #2

As support for the results of the first patient data simulation, a second patient simulation was performed. The patient data described in this section is recorded by Vlieg [27]. The simulation is set-up in the same way as described in the previous section, section 4.2.1. An overview of the patient data is given in Figure 45. Image (A) in this figure shows the PA result from the HTFI. Image (B) shows the US result and image (C) shows the overlay with the used tissue model in the simulation.

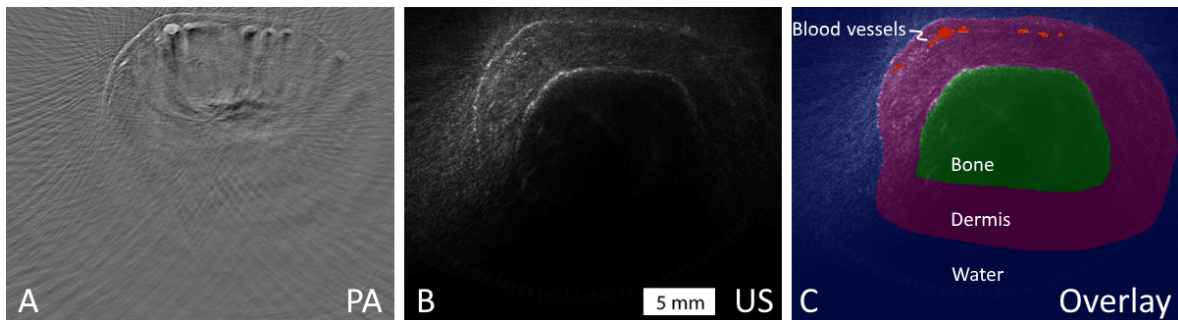


Figure 45: Results from Vlieg [27]. The image on the left hand side shows the photoacoustic image. The ultrasound image is shown in the center and the image on the right hand side shows the overlay with the patients tissue model used in the simulation.

The results following from the simulation are displayed in Figure 46. This figure shows the result from the simulation in image (A) and the original PA result from the HTFI in image (B). In the original result the signal from the skin is also reconstructed, as it contributed to the initial pressure. The simulation result only shows the blood vessels as only the initial pressure from the blood vessels was simulated. There is a dark region visible above the reconstructed blood vessels in the top of the image which does not appear in the original result. The shape and size of the streak artefacts from the simulation seem to be similar to the streak artefacts in the original result.

An overlay of both images is provided in Figure 47. The image on the left hand size (A) shows a blend of 50% of both images, the image on the right hand size (B) shows a blend of 30% for the simulation result and 70% for the original patients image. The result from the simulation is colorized to allow comparison between both images.

4. INVESTIGATION OF ACOUSTIC REFLECTION

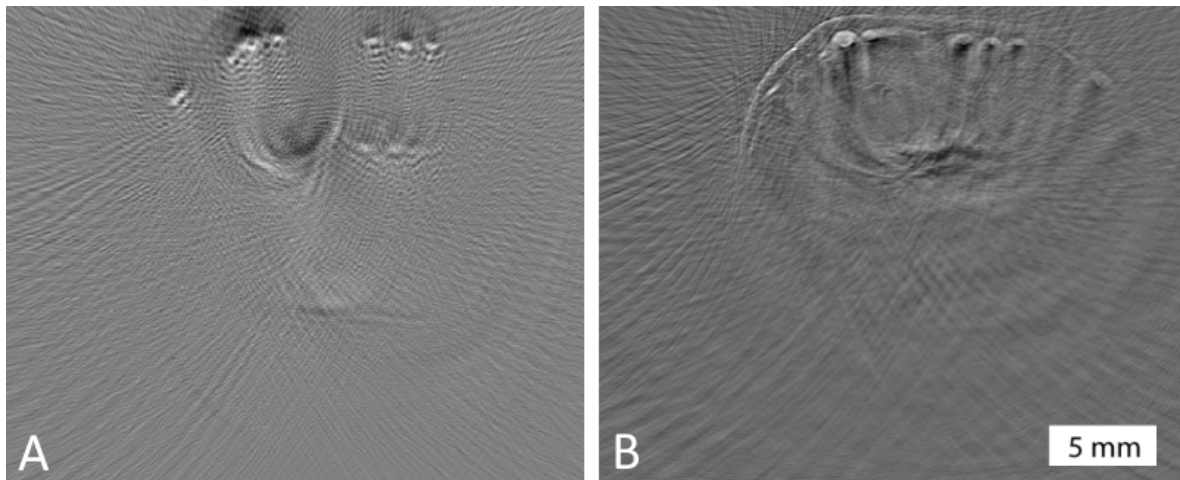


Figure 46: Result from the simulation is given in image (A) and the original PA result from the HTFI in image (B). When comparing the simulation result with the original result it also stands out that less visible blood vessels on the right hand side of the original result were not included in the initial pressure of the simulation.

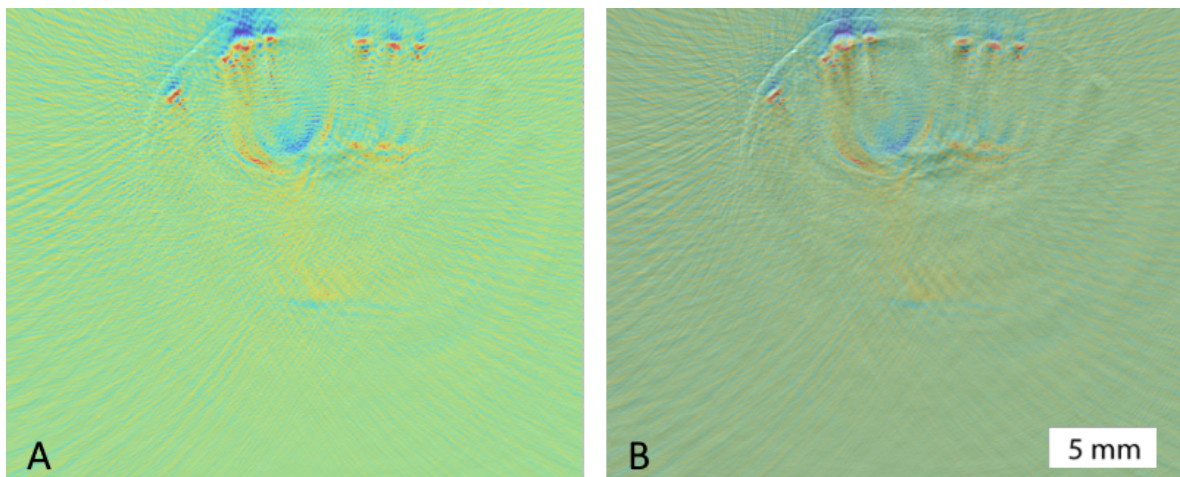


Figure 47: Two overlays of the original photoacoustic image from the patient and the result from the simulation. The image on the left hand side (A) shows a blend of 50%, the image on the right hand side shows a blend of 30% of the simulation result and 70% of the patients image.

4.3 Discussion

No numerical simulations were performed with smaller arbitrary bone shapes or larger blood vessels. Future investigations could include a rougher bone surface to more deeply investigate the effect of acoustic reflection and scattering on rough bone surface.

When observing the results from the patient simulations at first glance, the overlay of both images as shown in Figure 42 show similar results. It seems that most of the major streak artefacts as seen in the patients photoacoustic image, are also present in the same shape and size in the result of the simulation.

When observing the results from the simulation with different combinations of tissue types, as shown in Figure 44, differences can be distinguished. Both simulations without bone as shown in image (A) and (B) from Figure 44, show minor difference. The area under the reconstructed blood vessels shows some vertical negative lines, but these are as expected when performing time reversal with single projection. The result for the simulation with bone, as shown in image (C) from Figure 44, shows similarities with Figure 40 and the photoacoustic image from the patient as shown in image (B), Figure 41.

In the results from the simulation of the second patient case it stands out that blood vessels on the right hand side of the original photoacoustic image were not included in the simulation. This can be observed when viewing Figure 46. The excluding of these blood vessels is a result from the manual selection process to define the blood vessels in the simulation. In a future attempt to improve the simulation, a more robust selection method for the blood vessels can be implemented.

Although many similarities can be seen in the presented results, there are still several differences which can be observed between the simulated results and the patients results. For example, the simulated result has a large area with negative signal above and around the blood vessels, which is not seen in the original patients result. A definitive explanation for this difference is not found yet. It is suspected that the parameters in the k-Wave simulation (such as local attenuation and absorption settings) need further improvement to reduce the signal around the blood vessels. Also, it is important to note that simulated data which is assumed as the ground truth (such as the used tissue model) is never an exact copy of the original patient data. Another aspect is that the original initial pressure is unknown and an estimation is used in the simulation. The patients bone can have a rougher surface than simulated, which also introduces a deviation in the results. The last aspect is that the behavior of the simulated transducers will always deviate from the behavior of the transducers in the HTFI.

It is also important to note that the simulations were performed with help of the time reversal algorithm, while the photoacoustic image of the patient is reconstructed with the filtered back projection. Although it is explained and stated in section 1.2.2 that the result from the simulation approaches the result of the HTFI, it is not an exact copy.

4.4 Conclusion

It is found that the streak artefacts as observed in the patients photoacoustic image are directly related to the shape and size of the bone in the finger of the patient, in combination with the single projection used during measurements. The pressure waves arising from the blood vessels reflect and scatter on the surface of the bone, which on their turn cause the characteristic streak artefacts during the reconstruction of the PA image. The simulations show that the streak artefacts can be predicted and replicated when the location of the blood vessels and the shape and size of the bone in the imaged finger is known.

Chapter 5

3D Visualizations

The 3D visualization of the blood vessels in an imaged patient finger can be a powerful tool to give more insight in the behavior and severity of the disease state. This chapter covers all steps and choices made in order to build the 3D visualization algorithm.

5.1 Introduction

The growth of blood vessels around inflamed joints increases and with a tool to visualize the blood vessels in the finger, it would be potentially possible to monitor the progression of RA over time [13]. The tool presented in this chapter is able to provide a 3D visualization of the blood vessels in imaged fingers of patients.

The 3D visualization tool is build upon the capabilities of the HTFI, in which both the PA as the US images are used to build the visualization. The US images are used to determine the location of the dermis and the surface of the bone in the slice, while the blood vessels are extracted from the PA image. The next section describes all the steps of the algorithm.

5.2 Algorithm Layout

The algorithm is divided in different sections, of which the major parts are:

- Determination of the dermis and bone edges.
- Extraction of the region of interest from the PA images.
- Threshold to extract the blood vessels from the PA images.
- Visualization of the bone, dermis and blood vessels.

An overview of the algorithm is given in Figure 48. The overview starts at the top with the ultrasound images of the patient as input. The dermis and bone locations are determined from these US images and used to extract the region of interest (ROI) with the blood vessels from the PA images. The dermis, bone surface and the blood vessels are then visualized.

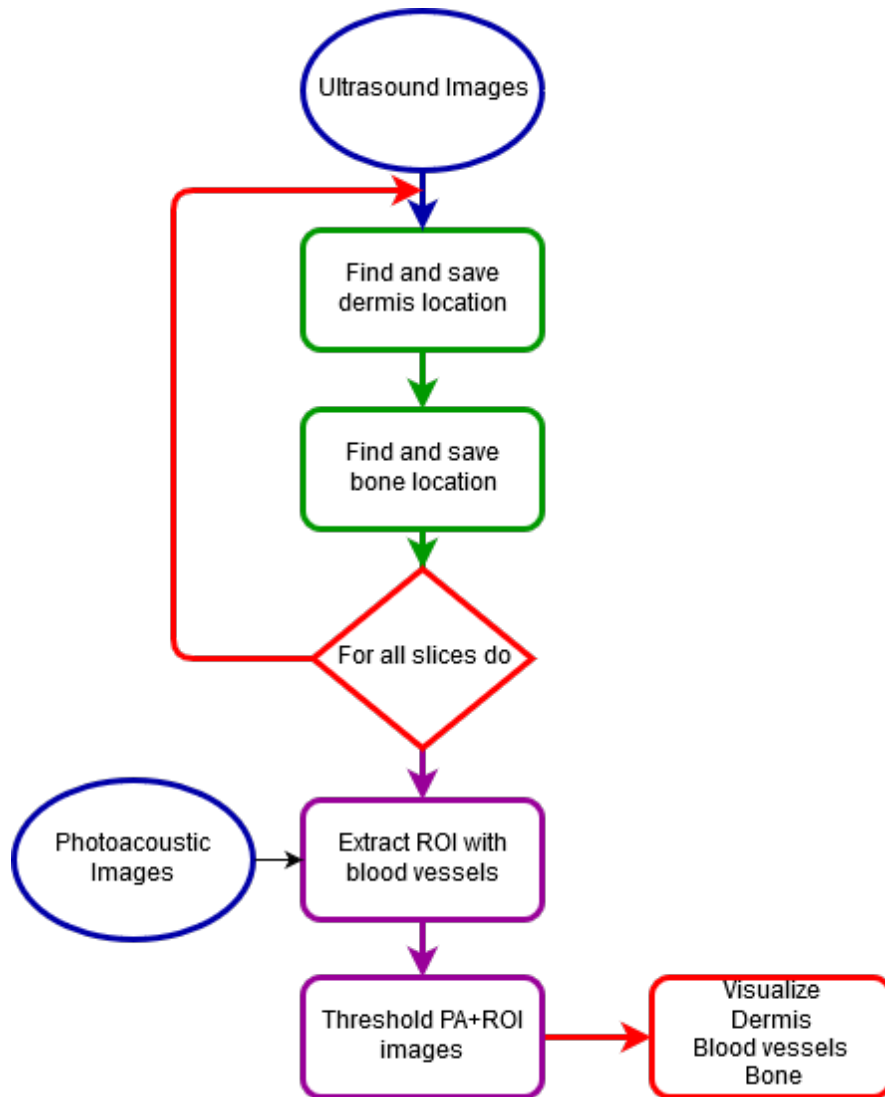


Figure 48: Schematic overview of the visualization algorithm. This overview starts at the top with the ultrasound images of the patient as input.

5.2.1 Extraction of the Dermis and Bone location

As described before, the location of the dermis and bone surface in each slice is determined with help of the US image of each slice. A double Gaussian derivative in the y-direction is used to enhance the surface of the dermis and bone from the background in the image. A threshold is then applied to the resulting image, in which only the pixels that fall in the top 5% of the intensity range are maintained. The threshold value was experimentally determined, where higher values were found to exclude too much information of the dermis and bone surface, while lower values tend to give more noise. An overview of these steps is given in Figure 49. In this figure the original US image is shown as (A), the Gaussian derived image in (B) and the resulting image with the applied threshold in (C).

Area filtering is then applied to the resulting image. This type of filter can be used to extract the bone and dermis layer by only maintaining the two largest connected white regions in the image. A curve is then plotted through the found surface locations of both the bone and the dermis. The plotted curve for both surfaces is used to extract the ROI from the PA image. The resulting ROI then only contains the blood vessels, where signal from the skin and from bone reflection is removed. An overview of these steps is given in Figure 49. The result from area filtering is shown in image (D). The found dermis locations are plotted as the red dots in image (E) and the resulting curves for both the dermis and bone surface are shown in image (F).

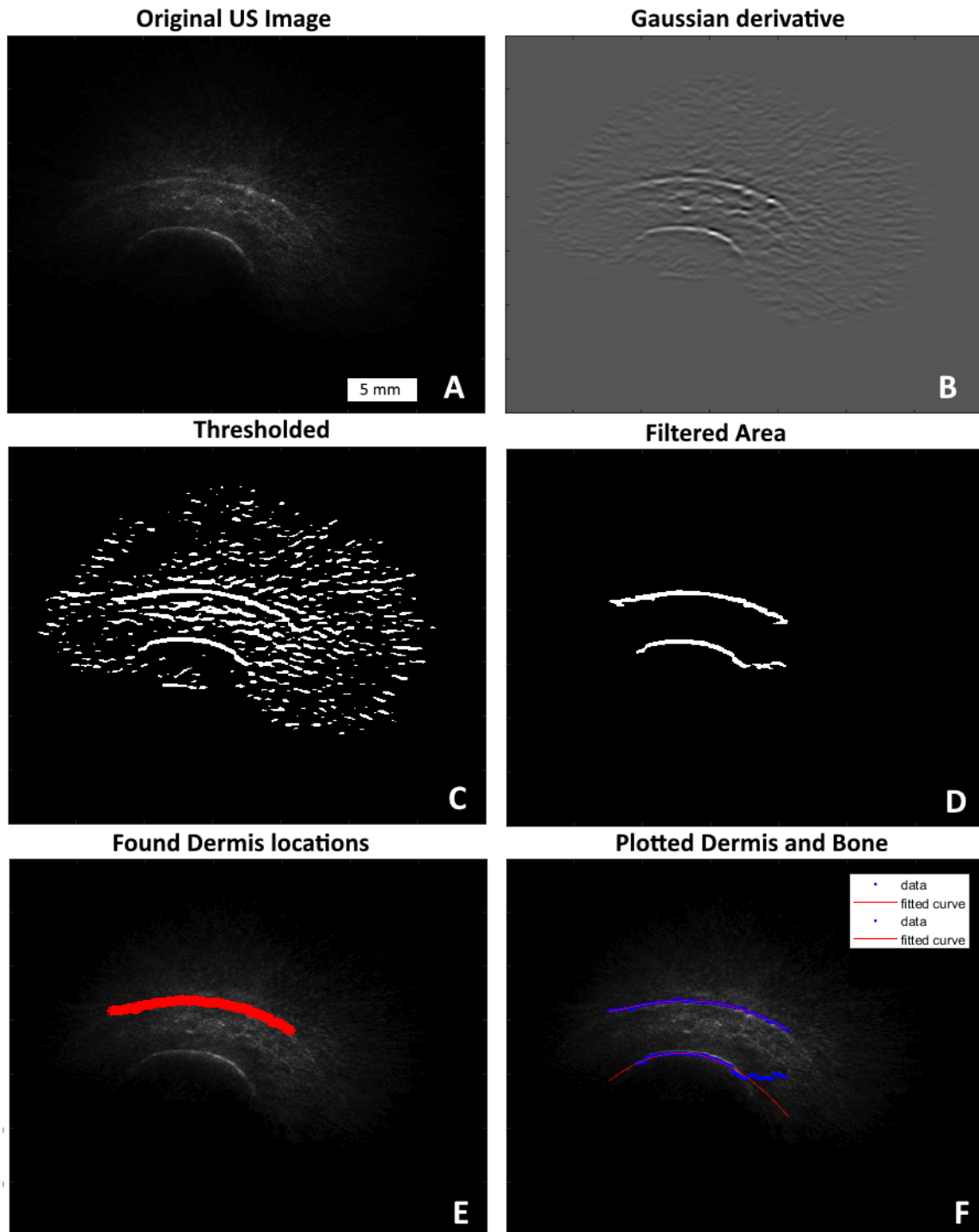


Figure 49: Overview of the steps to determine the bone and dermis surface from the US images. The original US image is shown as (A), the gaussian derivated image in (B) and the thresholded derivated image in (C). The result from area filtering is shown in image (D). The found dermis locations are plotted as the red dots in image (E). Image (F) shows the resulting curves in red for both the dermis and bone surface. The blue dots in image (F) are the found surface locations.

5.2.2 Extraction of the ROI

The most important part for the visualization is the determination of the region of interest which contains the blood vessels. The ROI is extracted from the original PA image of the slice with the help of the plotted curves from both the dermis as the bone surface as shown in image (F) of Figure 49. An overview of the original PA image and the resulting ROI is given in Figure 50. In this figure, image (A) shows the original PA image and image (B) shows the resulting ROI. It can be observed in image (B) that the parts of the image above and below the blood vessels are removed.

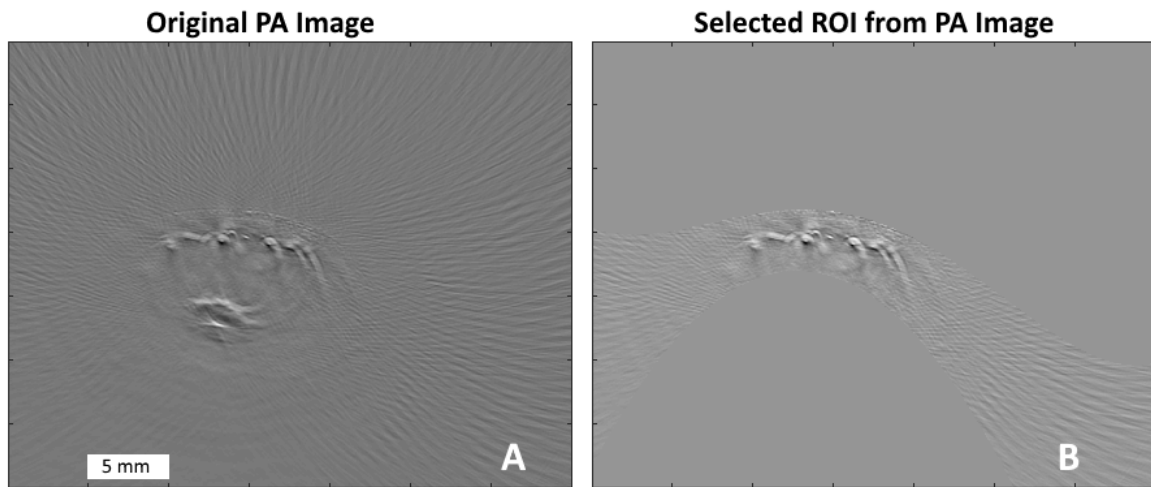


Figure 50: Overview of the selection of the ROI from the PA image. Image (A) shows the original PA image and image (B) shows the selected ROI.

5.2.3 Dermination of the blood vessels

The resulting ROI at this point does contains the information of the blood vessels and noise from the PA measurement. To speed up processing times in the visualization, the ROI is cut to a smaller size, which only contains the area of the blood vessels. The blood vessels can then be extracted from the ROI image by applying a threshold. This threshold is set to only maintain the pixels which fall within the top 1% of the intensity range from the ROI image. This threshold was determined by trial and error in which lower values were found to include too much background noise and higher values excluded information of blood vessel locations. An overview of the processed ROI image and the result from the application of the threshold is given in Figure 51. In this figure, image (A) shows the ROI after cropping and image (B) shows the resulting image after applying the threshold.

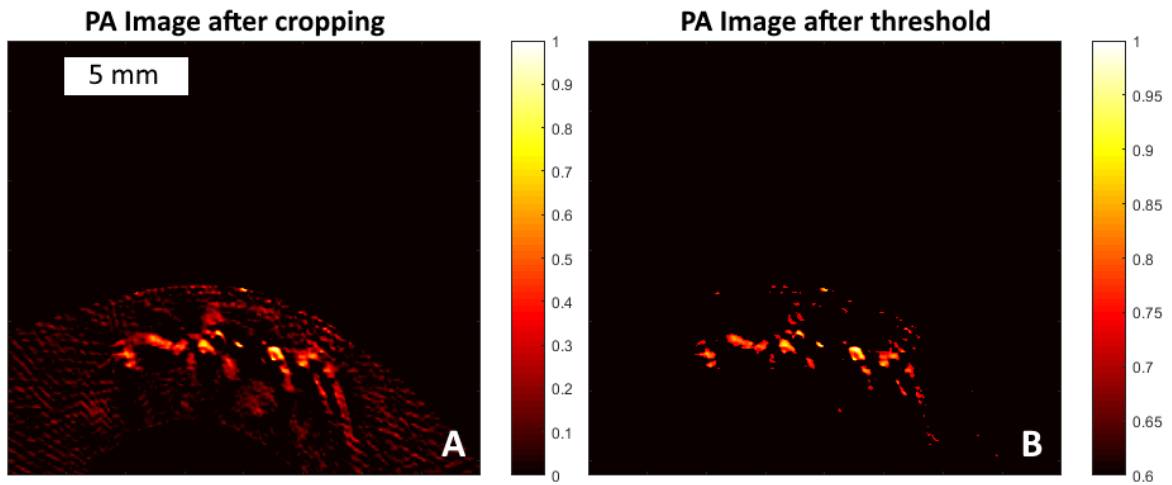


Figure 51: Overview of the steps necessary to extract the blood vessels. Image (A) shows the ROI after cropping and image (B) shows the resulting image after applying the threshold.

5.2.4 3D Visualization

All described steps are applied for all slices of the imaged finger. The results of every slice are stacked in a 3D matrix and this matrix can be visualized in Matlab. The visualization is performed by only coloring voxels in the 3D matrix which describe the dermis surface, blood vessels or bone surface. All other voxels are left blank.

The visualization is performed for two different cases. The first case is a healthy finger, without RA. The second case is an inflamed finger, which is affected by RA. The results are displayed in the next section.

5.3 Results

The results from the visualization algorithm are given in this section. Figure 52 shows the result of the 3D visualization of the blood vessels of the healthy case. In this figure, a frontal view and a side view with an horizontal angle of 45° from the frontal view is provided. The blood vessels are visualized in red and can be distinguished as the vertical cylindrical segments.

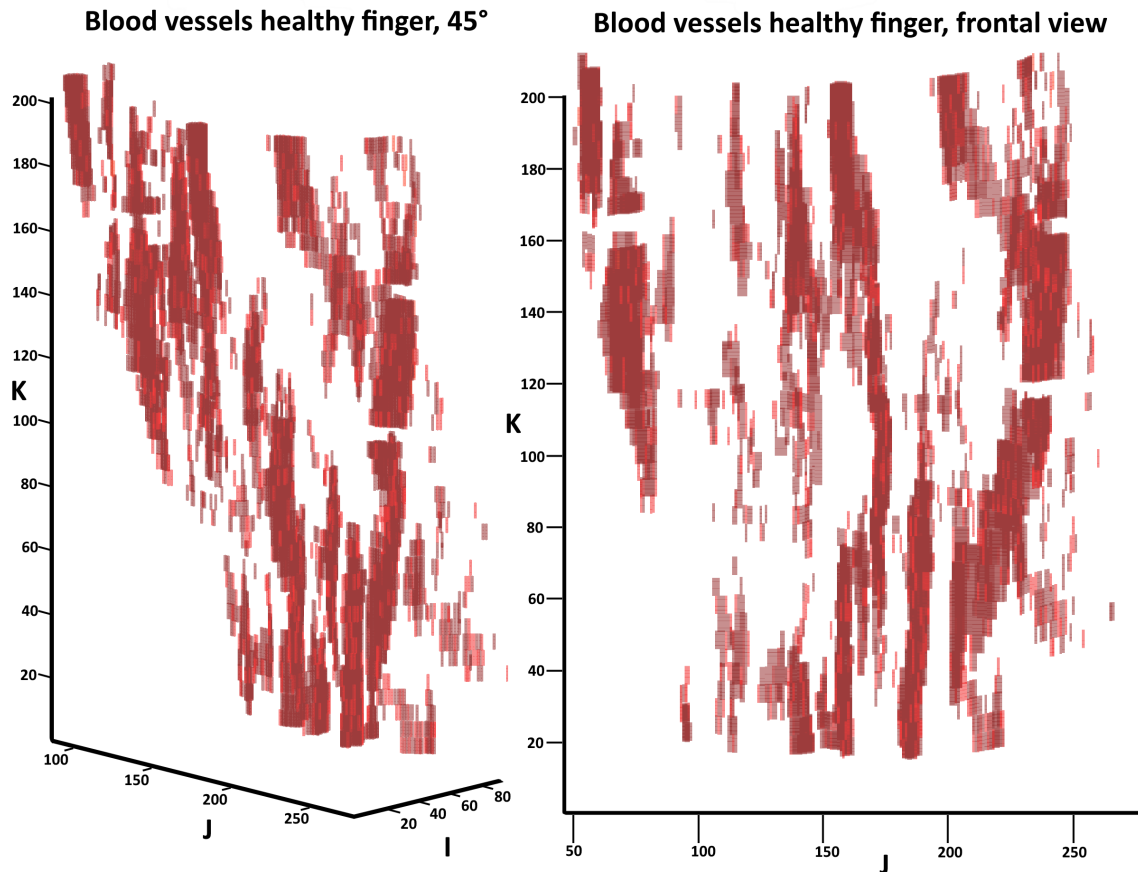


Figure 52: *Result of the visualization of the blood vessels for the case with the healthy finger. In this figure, a frontal view and a side view from an angle of 45° is given.*

Figure 53 shows the result of the visualization for the case with the inflamed finger which is affected by RA. As for the healthy case, a frontal view and a side view from an angle of 45° is provided.

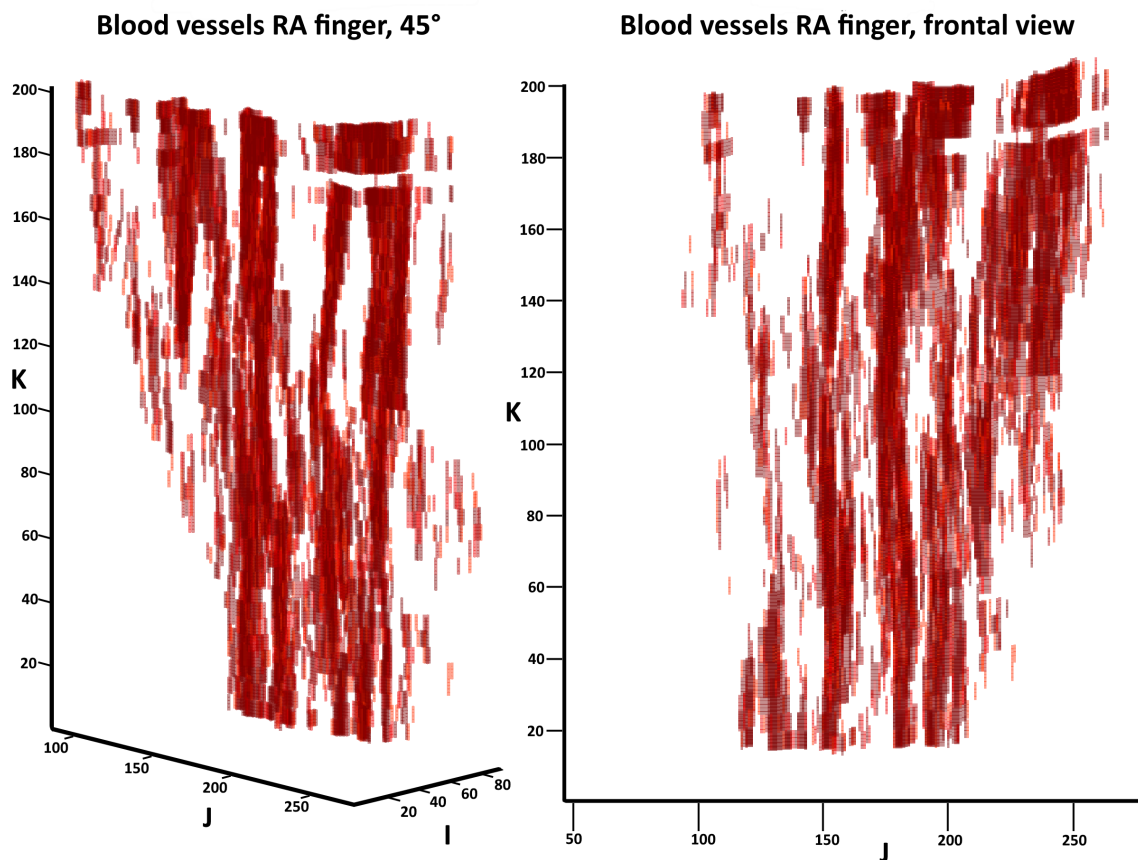


Figure 53: *Result of the visualization of the blood vessels for the case with the inflamed finger, affected by RA.*

The algorithm is also able to visualize the full imaged area of the finger with the dermis, blood vessels and bone surface. The results from the full visualization of the healthy case are given in Figure 54 and the results of the inflamed case in Figure 55. In both figures, the full visualization is given on the left hand side, with the bone surface in blue, the blood vessels in red and the dermis surface in green. The image in the center shows the visualization with only the bone surface and blood vessels. The image on the right hand side shows the visualization with only the dermis surface and blood vessels. All images are shown with a horizontal angle of -45° from the frontal view.

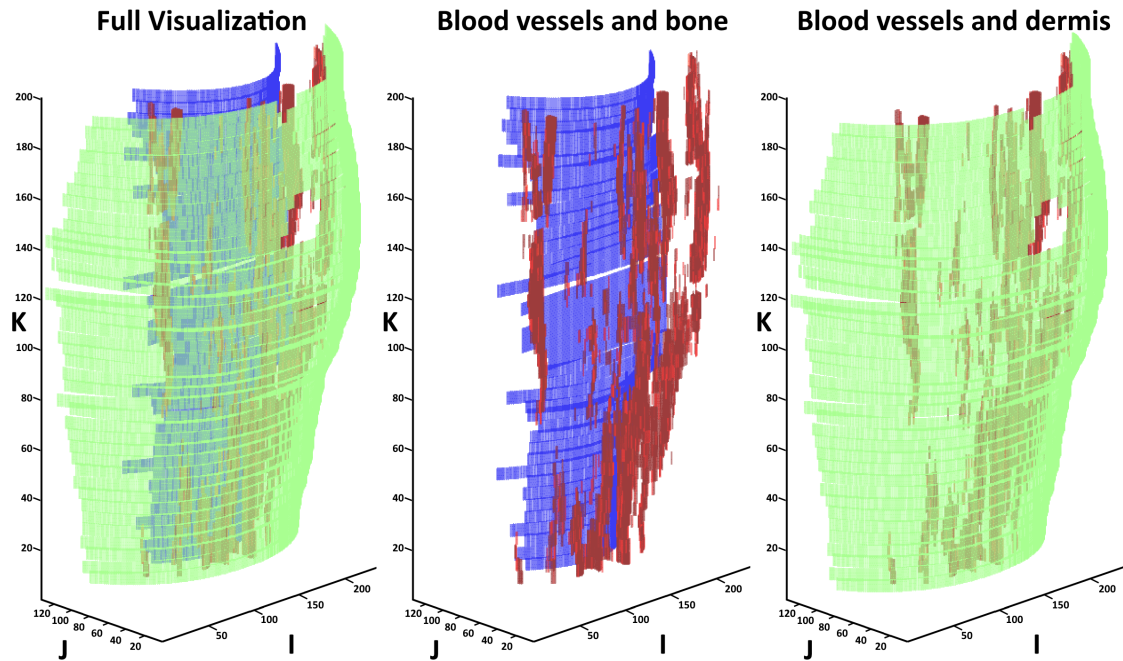


Figure 54: Result of the full visualization of the healthy case. The full visualization is given on the left hand side, with the bone surface in blue, the blood vessels in red and the dermis surface in green. The image in the middle shows the visualization with only the bone surface and the blood vessels. The image on the right hand side shows the visualization with only the dermis surface and the blood vessels. A gap in the dermis layer can be observed which is an effect of cropping the visualization result.

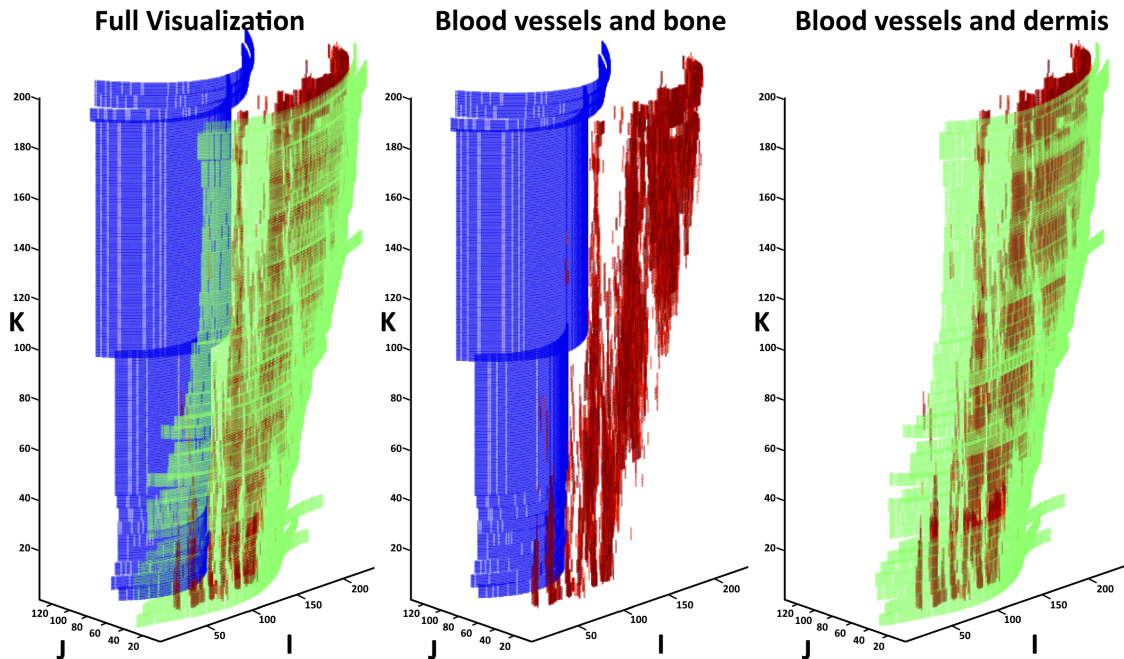


Figure 55: Result of the full visualization for the inflamed case. The full visualization is given on the left hand side, with the bone surface in blue, the blood vessels in red and the dermis surface in green. The image in the middle shows the visualization with only the bone surface and the blood vessels. The image on the right hand side shows the visualization with only the dermis surface and the blood vessels.

5.4 Discussion

The results shown in this section are from data sets both recorded by Vlieg [27]. It is important to note that the data sets are from the same patient (patient number 3). This patient had a severely inflamed finger, which was used as the inflamed case in this section. The healthy case in this section was data from a less inflamed finger, which was labeled as healthy in the thesis of Vlieg. These data sets were used due to the fact that they were recorded with single projection, contained 40 slices and were captured with a slice thickness of 0.5 mm, which had increased lateral resolution when compared with other available data sets.

The visualization of the blood vessels as given in Figure 52 shows that major blood vessels are distinguishable as the vertical cylindrical segments, but there is still noise present in the image. Parts of blood vessels seem to disappear and reappear again in the image. It is assumed that this is an effect of the heuristic applied threshold on the PA image for extracting the locations of the blood vessels.

When comparing Figure 52 and Figure 53, it stands out that the density of the blood vessels in the result of the inflamed case seems higher. There seem to be more blood vessels, but also more noise present in the images. The applied threshold for extracting the blood vessels from the PA images is kept equal for both the healthy as the inflamed case.

The segmentation algorithm used to determine the bone surface needs improvement. Currently a heuristic approach is implemented, which uses locations of the bone surface of previous slices if the algorithm fails to detect the surface of the bone in the current slice. An example of this effect is visualized in Figure 55, where the bone is plotted in blue. In this image it stands out that the algorithm failed to properly detect the surface of bone and used the location of the previous slice. This results in the cylindrical shape of the bone in the image. This effect is especially seen when comparing Figure 55 with Figure 54. As the algorithm was able to determine the surface of the bone in more slices for the healthy case, the bone shape is plotted as a more irregular surface in Figure 54. It is assumed that the more irregular plotted surface matches the real bone surface in the slices more closely.

5.5 Conclusion

From the results it can be concluded that it is possible to visualize the blood vessels in an imaged finger. There is a difference visible in vascularity and density of the blood vessels between a healthy and an inflamed case. This result fits the presented literature which states that the growth of blood vessels around inflamed joints increases. The presented tool is also able to segment and visualize the surface of the bone and dermis.

5.6 Outlook

The automatic segmentation algorithm is not robust and has room for improvement. Especially the detection of the edge of the bone in the US can be quite challenging due to low contrast in the images. Further improvement of the set threshold used for the extraction of the blood vessels could enhance the visualization by reducing artefacts in the final image. Another improvement for the visualization of the blood vessels would be to implement a statistical approach to connect loose elements and parts of blood vessels. This could be an approach to fill gaps and give more insight in how the blood vessels progress and meander through the finger tissue.

The visualization tool needs to be applied to more patient data sets to further improve the algorithm. When more data sets are analyzed and visualized, a more thorough conclusion can be drawn on the effectiveness of the visualization tool and the use of the algorithm in future patient follow-up. An example of patient follow-up would be visualization of the growth of blood vessels and tracking of the progression of RA over time.

References

- [1] Reumafonds, “Wat is Rheumatoïde artritis (RA)?” <http://www.reumafonds.nl/informatie-voor-doelgroepen/patienten/vormen-van-reuma/reumatoide-artritis/over-de-ziekte>, 2016. viewed on 2017-02-09.
- [2] G. S. Firestein, “Evolving concepts of rheumatoid arthritis,” *Nature* **423**(6937), pp. 356–361, 2003.
- [3] Centraal Bureau voor de Statistiek, Den Haag/Heerlen, “Overledenen; belangrijke doodsoorzaken (korte lijst), leeftijd, geslacht.” http://statline.cbs.nl/Statweb/publication/?DM=SLNL&PA=7052_95, 2016. viewed on 2016-12-16.
- [4] S.J. van der Linden (MUMC), M.J.J.C. Poos (RIVM), T. Hulshof, red. (RIVM), “Prevalentie van reumatoïde artritis.” <https://www.volksgezondheidszorg.info/onderwerp/reumato%C3%AFde-artritis-ra/cijfers-context/huidige-situatie#node-prevalentie-van-reumato%C3%AFde-artritis>, 2017. viewed on 2017-02-09.
- [5] M.J.J.C. Poos (RIVM), L.C.J. Slobbe (RIVM), “Kosten van zorg voor reumatoïde artritis.” <https://www.volksgezondheidszorg.info/onderwerp/reumato%C3%AFde-artritis-ra/kosten/kosten#node-kosten-van-zorg-voor-reumato%C3%AFde-artritis>, 2017. viewed on 2017-02-09.
- [6] Reumafonds, “Reuma in het kort / Wat is een gewricht?.” <http://www.reumafonds.nl/informatie-voor-doelgroepen/patienten/reuma-in-het-kort/wat-is-een-gewricht>, 2016. viewed on 2017-03-08.
- [7] K. H. Costenbader, D. Feskanich, L. A. Mandl, and E. W. Karlson, “Smoking intensity, duration, and cessation, and the risk of rheumatoid arthritis in women,” *The American journal of medicine* **119**(6), p. 503, 2006.
- [8] E. W. Karlson, L. A. Mandl, S. E. Hankinson, and F. Grodstein, “Do breast-feeding and other reproductive factors influence future risk of rheumatoid arthritis?: Results from the nurses’ health study,” *Arthritis & Rheumatism* **50**(11), pp. 3458–3467, 2004.
- [9] S.J. van der Linden (MUMC), M.J.J.C. Poos (RIVM), “Oorzaken reumatoïde artritis.” <https://www.volksgezondheidszorg.info/onderwerp/reumato%C3%AFde-artritis-ra/cijfers-context/oorzaken-en-gevolgen#node-oorzaken-reumato%C3%AFde-artritis>, 2017. viewed on 2017-02-09.
- [10] D. Aletaha, T. Neogi, A. J. Silman, J. Funovits, D. T. Felson, C. O. Bingham, N. S. Birnbaum, G. R. Burmester, V. P. Bykerk, M. D. Cohen, *et al.*, “2010 rheumatoid arthritis classification criteria: an american college of rheumatology/european league against rheumatism collaborative initiative,” *Arthritis & Rheumatism* **62**(9), pp. 2569–2581, 2010.

-
- [11] A. Klauser, F. Frauscher, M. Schirmer, E. Halpern, L. Pallwein, M. Herold, G. Helweg, and D. ZurNedden, "The value of contrast-enhanced color doppler ultrasound in the detection of vascularization of finger joints in patients with rheumatoid arthritis," *Arthritis & Rheumatology* **46**(3), pp. 647–653, 2002.
- [12] P. van Es, S. K. Biswas, H. J. B. Moens, W. Steenbergen, and S. Manohar, "Initial results of finger imaging using photoacoustic computed tomography," *Journal of biomedical optics* **19**(6), pp. 060501–060501, 2014.
- [13] G. S. Firestein, "Starving the synovium: angiogenesis and inflammation in rheumatoid arthritis," *The Journal of clinical investigation* **103**(1), pp. 3–4, 1999.
- [14] M. Hau, C. Kneitz, H. Tony, M. Keberle, R. Jahns, and M. Jenett, "High resolution ultrasound detects a decrease in pannus vascularisation of small finger joints in patients with rheumatoid arthritis receiving treatment with soluble tumour necrosis factor α receptor (etanercept)," *Annals of the Rheumatic Diseases* **61**(1), pp. 55–58, 2002.
- [15] A. Marrelli, P. Cipriani, V. Liakouli, F. Carubbi, C. Perricone, R. Perricone, and R. Giacomelli, "Angiogenesis in rheumatoid arthritis: a disease specific process or a common response to chronic inflammation?," *Autoimmunity reviews* **10**(10), pp. 595–598, 2011.
- [16] M. Xu and L. V. Wang, "Photoacoustic imaging in biomedicine," *Review of scientific instruments* **77**(4), p. 041101, 2006.
- [17] S. Hu and L. V. Wang, "Photoacoustic imaging and characterization of the microvasculature," *Journal of biomedical optics* **15**(1), pp. 011101–011101, 2010.
- [18] P. Beard, "Biomedical photoacoustic imaging," *Interface focus* , p. rsfs20110028, 2011.
- [19] S. A. Prahl, "Optical Absorption of Hemoglobin ." <http://omlc.org/spectra/hemoglobin/>, 1999. viewed on 2017-04-11.
- [20] X. Wang, Y. Xu, M. Xu, S. Yokoo, E. S. Fry, and L. V. Wang, "Photoacoustic tomography of biological tissues with high cross-section resolution: Reconstruction and experiment," *Medical physics* **29**(12), pp. 2799–2805, 2002.
- [21] K. P. Köstli and P. C. Beard, "Two-dimensional photoacoustic imaging by use of fourier-transform image reconstruction and a detector with an anisotropic response," *Applied optics* **42**(10), pp. 1899–1908, 2003.
- [22] Y. Hristova, P. Kuchment, and L. Nguyen, "Reconstruction and time reversal in thermoacoustic tomography in acoustically homogeneous and inhomogeneous media," *Inverse Problems* **24**(5), p. 055006, 2008.
- [23] X. Liu and D. Peng, "Regularized iterative weighted filtered back-projection for few-view data photoacoustic imaging," *Computational and Mathematical Methods in Medicine* **2016**, 2016.
- [24] B. E. Treeby and B. T. Cox, "k-wave: Matlab toolbox for the simulation and reconstruction of photoacoustic wave fields," *Journal of biomedical optics* **15**(2), pp. 021314–021314, 2010.

REFERENCES

- [25] P. Zhang, X. Zhang, and G. Fang, “Comparison of the imaging resolutions of time reversal and back-projection algorithms in em inverse scattering,” *IEEE Geoscience and Remote Sensing Letters* **10**(2), pp. 357–361, 2013.
- [26] L. M. Zwiers, “Photoacoustic tomography for finger joint imaging: Identification, evaluation and removal of artefacts,” *Master Thesis* , 2016.
- [27] R. C. Vlieg, “Tomography imaging setup to measure inflammation in the finger using ultrasound and photoacoustics,” *Master Thesis* , 2016.
- [28] P. van Es, R. C. Vlieg, E. Hondebrink, J. C. van Hespren, H. J. B. Moens, W. Steenbergen, and S. Manohar, “Coregistered photoacoustic and ultrasound tomography of healthy and inflamed human interphalangeal joints,” in *European Conference on Biomedical Optics*, p. 95390C, Optical Society of America, 2015.
- [29] P. Van Es, S. Biswas, H. B. Moens, W. Steenbergen, and S. Manohar, “Photoacoustic tomography of the human finger: towards the assessment of inflammatory joint diseases,” in *SPIE BiOS*, pp. 93234Q–93234Q, International Society for Optics and Photonics, 2015.
- [30] J. Xia and L. V. Wang, “Small-animal whole-body photoacoustic tomography: a review,” *IEEE Transactions on Biomedical Engineering* **61**(5), pp. 1380–1389, 2014.
- [31] D. Piras, W. Xia, W. Steenbergen, T. G. van Leeuwen, and S. Manohar, “Photoacoustic imaging of the breast using the twente photoacoustic mammoscope: present status and future perspectives,” *IEEE Journal of Selected Topics in Quantum Electronics* **16**(4), pp. 730–739, 2010.
- [32] G. Xu, J. R. Rajian, G. Girish, M. J. Kaplan, J. B. Fowlkes, P. L. Carson, and X. Wang, “Photoacoustic and ultrasound dual-modality imaging of human peripheral joints,” *Journal of biomedical optics* **18**(1), pp. 010502–010502, 2013.
- [33] J. Jo, G. Xu, J. Hu, A. Marquardt, J. Yuan, G. Girish, X. Wang, *et al.*, “Optimizing the optical wavelength for the photoacoustic imaging of inflammatory arthritis,” in *SPIE BiOS*, pp. 93230B–93230B, International Society for Optics and Photonics, 2015.
- [34] J. Jo, G. Xu, A. Marquardt, S. Francis, J. Yuan, D. Girish, G. Girish, and X. Wang, “Photoacoustic imaging of inflammatory arthritis in human joints,” in *SPIE BiOS*, pp. 96894H–96894H, International Society for Optics and Photonics, 2016.
- [35] S. Preisser, G. Held, H. G. Akarçay, M. Jaeger, and M. Frenz, “Study of clutter origin in in-vivo epi-optoacoustic imaging of human forearms,” *Journal of Optics* **18**(9), p. 094003, 2016.
- [36] V. Del Grosso and C. Mader, “Speed of sound in pure water,” *the Journal of the Acoustical Society of America* **52**(5B), pp. 1442–1446, 1972.
- [37] M. O. Culjat, D. Goldenberg, P. Tewari, and R. S. Singh, “A review of tissue substitutes for ultrasound imaging,” *Ultrasound in medicine & biology* **36**(6), pp. 861–873, 2010.
- [38] D. P. Landau and K. Binder, *A guide to Monte Carlo simulations in statistical physics*, Cambridge university press, 2014.

- [39] S. L. Jacques, “Coupling 3d monte carlo light transport in optically heterogeneous tissues to photoacoustic signal generation,” *Photoacoustics* **2**(4), pp. 137–142, 2014.
- [40] S. L. Jacques, S. A. Prahl, “Henyey-Greenstein scattering function.” <http://omlc.org/education/ece532/class3/hg.html>, 1998. viewed on 2017-02-21.
- [41] V. Periyasamy and M. Pramanik, “Monte carlo simulation of light transport in tissue for optimizing light delivery in photoacoustic imaging of the sentinel lymph node,” *Journal of biomedical optics* **18**(10), pp. 106008–106008, 2013.
- [42] G. S. Kell, “Density, thermal expansivity, and compressibility of liquid water from 0. deg. to 150. deg.. correlations and tables for atmospheric pressure and saturation reviewed and expressed on 1968 temperature scale,” *Journal of Chemical and Engineering Data* **20**(1), pp. 97–105, 1975.
- [43] B. Treeby, B. Cox, “k-Wave Toolbox: Modelling Sensor Directivity in 3D Example.” http://www.k-wave.org/documentation/example_sd_directivity_modelling_3D.php, 2009. viewed on 2017-05-31.

Appendix

A Monte Carlo number of photons investigation

The number of photons used in the Monte Carlo simulation as described in section 3.1 determines the simulation time needed and robustness of the final result. The simulation was performed for several different numbers of photons to find an optimal trade-off between the simulation time and the robustness of the result.

Figure 56 gives an overview of results from the Monte Carlo simulation with different amounts of photons. The simulation was performed with $1.5e^3$, $1.5e^4$, $1.5e^5$ and $1.5e^6$ photons. The figures show that with an increasing amount of photons simulated, the number of photons absorbed in the tissue model (at height z is 7 cm) also increases.

Figure 57 gives an overview of the intensity plot. This intensity plot is taken along the line y is 0 cm and starts from z is 5 cm to z is 7 cm in the plots of Figure 56. The results in the graph show that the data points for both the results of $1.5e^3$ and $1.5e^4$ are not connected, as not all pixels along the intensity line have a value. The amounts of $1.5e^3$ and $1.5e^4$ photons is not sufficient to fill all pixels and provide a smooth image and are thus not good candidates as the number of photons to be simulated in the Monte Carlo simulation. The results for $1.5e^5$ and $1.5e^6$ photons show that the noise and difference between neighboring pixel intensities decreases with increasing number of photons simulated.

Figure 58 shows the correlation between the amount of photons simulated and the time needed to perform the simulation. The simulation is able to simulate $1.025e^5$ photons per minute. This makes that the simulation of $1.5e^3$ photons takes 0.029 min or 1.74 seconds. The simulation with $1.5e^6$ photons takes 14.6 minutes.

Although the results show that there is still some noise present in the images, the amount of $1.5e^6$ photons was assumed to give a sufficient simulation result with a reasonable simulation time.

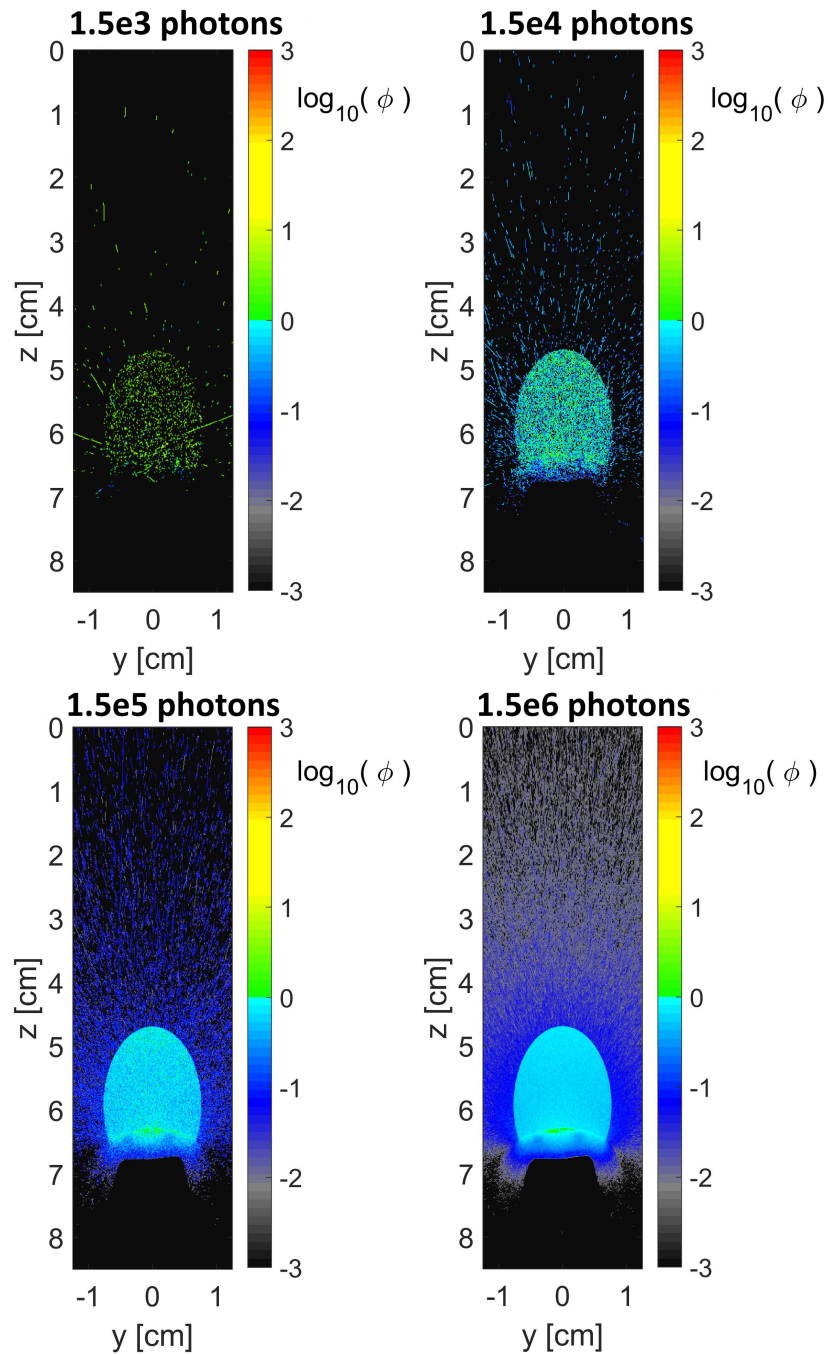


Figure 56: Results from the Monte Carlo simulation with different amounts of simulated photons. The images shown represent the fluence map of the simulation at the plane x is 0 cm.

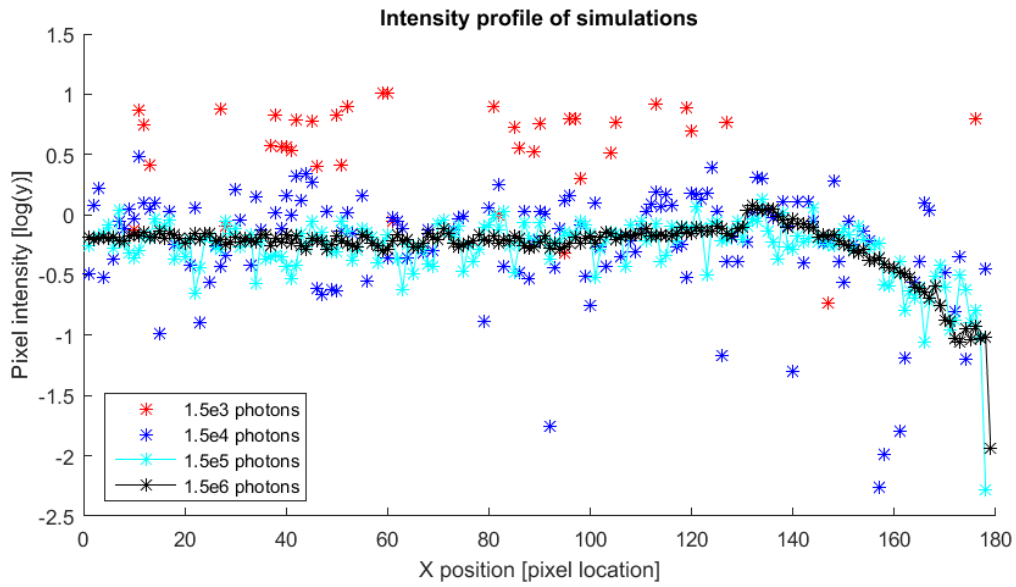


Figure 57: Profile plot of the simulation results from the different amount of simulated photons. The local pixel intensity is given as $\log(y)$ on the y-axis. The pixel location along the line used for the profile plot is given on the x-axis. Red: $1.5e3$ photons simulated. Dark blue: $1.5e4$ photons. Cyan: $1.5e5$ photons. Black: $1.5e6$ photons.

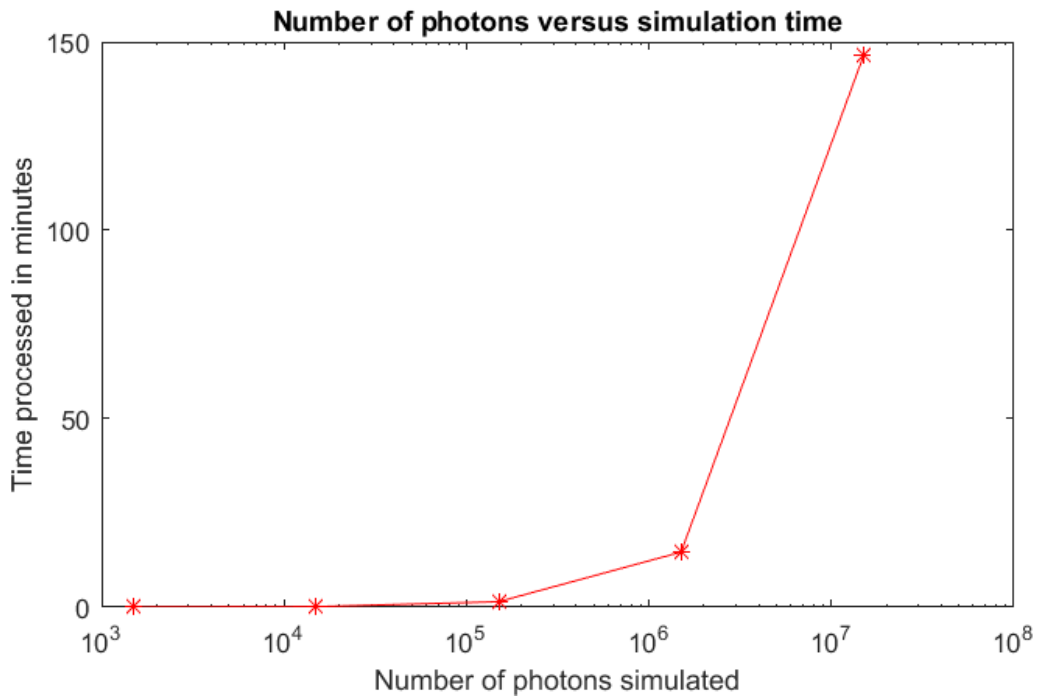


Figure 58: Overview of the correlation between number of photons simulated and the time needed to perform the simulation. The number of photons simulated are given on the logarithmic x-axis. The time needed to perform the simulation is given in minutes on the y-axis.

B Effect of k-Wave filtering

Section 3.3 describes the use of a Gaussian filter (Figure 30) on the recorded signal of the k-Wave simulation. Figure 59 provides an overview of the results of the k-Wave simulation with and without filtering. This figure shows the two patient simulations with filtering on the left hand side and the unfiltered results of the simulation on the right hand side. Patient number one and two refer to the patient cases as described in section 4.2.

In these images it stands out that the results without filtering seem blurred when compared to the filtered results. When comparing images (A) and (B) the dark (negative) area directly above the blood vessels seems to be larger in the unfiltered result. It stands out that the streak artefacts directly beneath the reconstructed blood vessels in the filtered images seem less smooth than the unfiltered results and small ripple-like artefacts can be observed in the streak artefacts due to the effect of filtering.

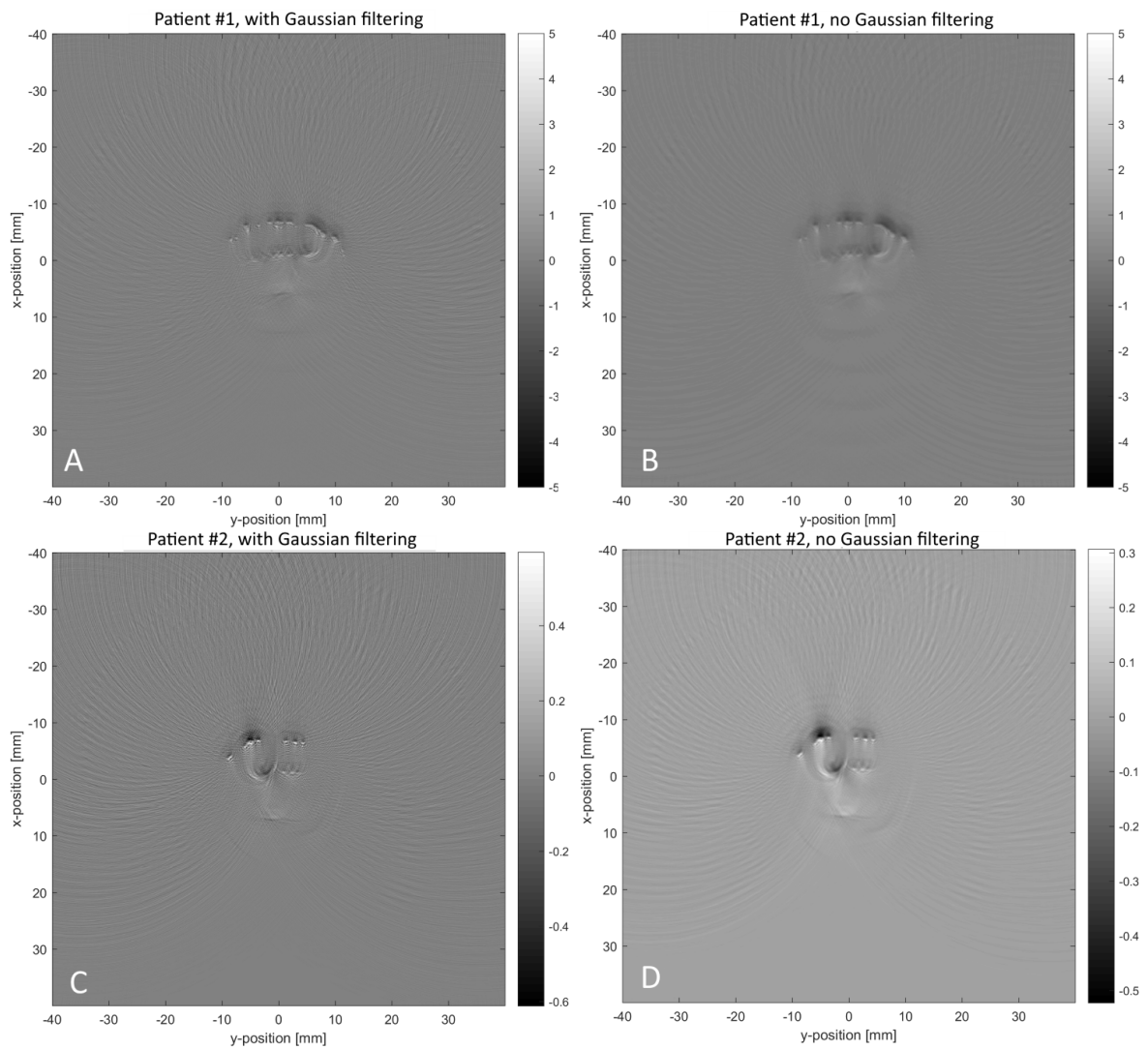


Figure 59: Results of the *k*-Wave patient simulations with and without the application of the Gaussian filter. Images (A) and (C) show the patient result with filtering. Images (B) and (D) show the unfiltered simulation result.